Open Access

Recent Progress in Materials

LIDSEN Publishing Inc.

Research Article

Optical, Charge Transport, Thermal, Magnetic, Plasmonic, and Quantum Mechanical Properties of Iridium

William E Vargas [1, *], Federico Muñoz-Rojas [1], Esteban Avendano [1], Victoria Quirós-Cordero [2], Marcela Hernández-Jiménez [1]

1. Centro de Investigación en Ciencia e Ingeniería de Materiales, Universidad de Costa Rica, San José, Costa Rica; E-Mails: william.vargascastro@ucr.ac.cr; federico.munozrojas@ucr.ac.cr; esteban.avendanosoto@ucr.ac.cr; marcela.hernandezjimenez@ucr.ac.cr
2. School of Materials Science and Engineering, College of Engineering, Georgia Institute of Technology, Atlanta, Georgia, United States; E-Mail: victoria.quiroscordero@gatech.edu

* **Correspondence:** William E. Vargas; E-Mail: william.vargascastro@ucr.ac.cr

Academic Editor: Vardan Apinyan

Special Issue: Quantum Mechanics in Solid State Systems

Recent Progress in Materials
2022, volume 4, issue 4
doi:10.21926/rpm.2204019

Received: July 30, 2022
Accepted: September 23, 2022
Published: October 12, 2022

Abstract

Spectrophotometry has been widely used to retrieve the dielectric function of a bulk iridium sample using an extended version of the Drude–Lorentz model. The parameters of the model are optimized using a spectral-projected-gradient-method-assisted acceptance-probability-controlled simulated annealing approach. Furthermore, optimized values of Drude parameters corresponding to the optical response of electrons and holes (scattering frequency of electrons, the ratio between scattering frequencies of holes and electrons, the ratio between effective masses of electrons and holes, the ratio between the number densities of holes and electrons, and electron volume plasma frequency) are used to evaluate charge transport and magnetic properties. These include static and dynamic conductivities, intrinsic mean free paths, the effective mass of charge carriers and their number densities, Fermi velocities and energies, densities of states at Fermi energies, mobilities, specific heats, Hall's coefficient, thermal conductivities, charge carrier coupling constant, paramagnetic and

diamagnetic susceptibilities, and the number of Bohr magnetons. In addition, optimized resonance energy values of the Lorentz contribution to the dielectric function were compared with the background information provided by density-functional-theory calculations for iridium. A decomposition of the energy loss function was used as the starting point to calculate the effective numbers of bound electrons involved in interband transitions, as well as the densities of states at the final energies of the sets of transitions considered. The Drude–Lorentz model involves charge carrier parameters for both electrons and holes, as well as the resonance energies correlating with the energies associated with quantum transitions. To a large extent, several physical quantities calculated from optimized parameters exhibit values close to those obtained from measurements or by applying other models, including quantum mechanics formulations.

Keywords
Charge transport; reflectivity; density of states; magnetic susceptibility; Drude–Lorentz model; electron localization; iridium; density functional theory; simulated annealing

1. Introduction

The transition metal iridium (Ir) has been increasingly used in the industry due to its physical properties, including high mechanical strength, low oxidation at ambient conditions, corrosion resistant, large work function, high melting point, and high electrical conductivity. It has been widely applied in thermocouples and as an encapsulating material to stabilize and provide mechanical protection to radioisotopes used as nuclear fuels [1], in microelectronics for designing and implementing dynamic- and ferroelectric- random access memory electrodes [2], as gate electrodes in metal-oxide-semiconductor field-effect transistors [3], and as ohmic contact in diamond-based electronic devices [4], as coatings in spatial instrumentation to protect against ultraviolet radiation [5], in gas sensors [6] and catalytic processes [7, 8]. In addition, Ir has been implicated in the design and characterization of metallic photonic-band-gap crystals [9]. Iridium oxide has been used in optically variable electrochromic materials used in smart windows [10], as an electrode catalytic material in water electrolysis [11], and in several other industrial and technological applications [12].

The optical, charge-carrier transport, and magnetic properties, as well as band structure calculations of Ir have not been well studied. Reports on the optical properties of Ir are scarce, with the first study reported in 1910, which focused on metal mirrors containing the measured spectral reflectivity of Ir for near- and mid-infrared wavelengths [13]. In 1966, a study on the optical constants and emissivity of heated semicircular filaments of refractory metals, including Ir, for near-infrared and visible photon energies was published [14]. A year later, the optical constants of Ir films were obtained from the inversion of reflection measurements in a vacuum ultraviolet spectral range [15]. Moreover, the reflection and transmission of ultraviolet radiation by Ir thin films became a popular research topic [16]. Similarly, optical constants retrieved from reflectivity measurements for near-infrared, visible, and near-ultraviolet energies were reported in 1972 [17]. Weaver et al. used an extended spectral range [18-20] to obtain the dielectric function of bulk Ir from absorptivity and reflectivity measurements using a wide spectrum ranging from near-infrared to vacuum

ultraviolet energies (0.2 to 40 eV). The optical constants of electron-beam evaporated Ir films were obtained from extreme ultraviolet to X-rays spectral ranges [21]. Refractive index and extinction coefficients of dc magnetron sputtered/atomic-layer-deposited Ir thin films were obtained using ellipsometry in the spectral range from the middle/near-infrared to vacuum/near ultraviolet [22, 23]. Recently, the Ir optical constants in the visible, ultraviolet, and X-ray energy ranges, obtained from inversion of reflected electron energy loss spectra, have been published [24] (2 to 200 eV). Furthermore, the literature on band structure calculations for Ir is scarce. Characterizations of cross sections of the Fermi surface were initially reported [25, 26], with band structure diagrams obtained using a Relativistic Augmented Plane Wave method [27]. Noffke and Fritsche [28] reported the total density of states (DOS) and the contributions from *s*, *p*, *d*, and *f* states, with similar results reported in more recent publications [29-31].

The primary purpose of the present study is to model the dielectric function (DF) of Ir for a polycrystalline bulk sample with known dielectric function obtained from absorptivity measurements at low temperature (for energies between 0.2 and 4.4 eV), and from reflectivity spectra at room temperature (RT) for energies between 3 and 40 eV [18-20]. The modeling was performed using an extended version of the Drude–Lorentz model, incorporating the contribution of electrons and holes in the Drude term, whose parameters are calculated from an optimization procedure based on a Spectral Projected Gradient Method (SPGM)-assisted Acceptance Probability Controlled Simulated Annealing (APCSA) approach. The same approach has been applied to Rh [32]. Using the optimized values of Drude parameters and the relative number density of conduction electrons, a set of derived physical quantities were evaluated for conduction electrons and holes, including effective masses, relaxation times, mobilities, Fermi energies, DOS at the Fermi energies, Fermi velocities, mean free paths, thermal conductivities, specific heats, magneton numbers, paramagnetic and diamagnetic susceptibilities, Hall's coefficient, and hole and electron conductivities. We use our density-functional-theory (DFT) calculations, performed with the inclusion of the spin-orbit coupling, to interpret the Fermi energies and corresponding DOS values as background evaluations of the spectral dependence of the DOS and the band structure diagram for Ir. The resonance frequencies involved in the Lorentz contribution to the dielectric function were initially estimated from reported photometric studies. Because most spectral measurements were recorded at RT, we considered that the dielectric function, optimized parameters, and those that are derived corresponded to their values at RT.

Section 2 summarizes the formulation of the model, describing the parameters to be optimized and those obtained as derived quantities. Section 3 reports the characterization of Ir from the point of view of band structure calculations. Section 4 presents the modeling of the dielectric function of the sample previously mentioned whose dielectric function was obtained from the literature. Section 5 analyzes the approach from the band structure calculations to estimate the density of states and Fermi energies of itinerant electrons and holes charge carriers to compare with the evaluations based on the SPGM-APCSA optimization. Decompositions of bulk and surface energy loss functions (ELFs) are considered in Section 6. Evaluations of effective numbers of charge-carriers and electrons participating in each interband transition are reported in Section 7. Section 8 describes the decomposition of the Lorentzian ELF performed to estimate the density of states at the final energies corresponding to each set of transitions. A final summary and conclusions are given in the last Section.

2. Dielectric Function Model and Optimization Parameters

An extended version of the Drude–Lorentz (DL) model is obtained when we consider the contribution of conduction electrons and holes in the Drude term of the DF ($\varepsilon = \varepsilon_1 + i\varepsilon_2$) and incorporate the polarization and absorption due to bound electrons [33, 34]:

$$\varepsilon = \varepsilon_{hf} - \frac{1}{\Omega}\left(\frac{\Omega_{pe}^2}{\Omega + i\gamma_{oe}} + \frac{\Omega_{ph}^2}{\Omega + i\gamma_{oh}}\right) + \frac{1}{z_e}\sum_{j=1}^{K}\frac{f_j\Omega_{pe}^2}{\Omega_j^2 - \Omega^2 - i\Omega\gamma_j}, \quad (1)$$

where ε_{hf} is the high-frequency dielectric constant associated with the high energy interband transitions spectrally located beyond the energy range considered; $\Omega = h\omega/2\pi = h\nu$, where ν (ω) is the frequency (angular frequency) of the incident light; $\Omega_{pe} = h\nu_{pe}$ ($\Omega_{ph} = h\nu_{ph}$), with $\omega_{pe} = 2\pi\nu_{pe}$ ($\omega_{ph} = 2\pi\nu_{ph}$) as the volume plasma frequency of the collective oscillation of electrons (holes) whose scattering frequency is γ_{oe} (γ_{oh}), with h as Planck's constant; and $\omega_{pe} = (n_e e^2/\varepsilon_o m_e)^{1/2}$ with ε_o as the free space permittivity, e as the electron's charge, n_e as the number density of conduction electrons, and m_e as their effective mass. The scattering frequencies, γ_{oe} and γ_{oh} for electrons and holes, respectively, are related to corresponding relaxation times: $\tau_{oe} = h/2\pi\gamma_{oe}$ and $\tau_{oh} = h/2\pi\gamma_{oh}$. The relative number density of conduction electrons, i.e., the number of conduction electrons per atom, is $z_e = n_e/N$ with N as the number density of metal ions. N can be calculated from a, the lattice constant, and the number of atoms per conventional unit cell. Iridium has a face-centered cubic (fcc) structure with a = 0.3839 nm at RT [35], with four atoms per conventional unit cell [$N = 4/V_{cc}$ with $V_{cc} = a^3$ as the volume of the conventional unit cell]. It gives $N = 7.07 \times 10^{22}$ atoms/cm^3 for Ir.

The formulation of DF given by Equation (1) has the following advantages with respect to the traditional form of applying DL models: (1) the energy dependence of the Drude term, denoted as D(ε), is self-consistent with the physical behavior required when the angular frequency tends to zero. It allows to obtain the static conductivity and corresponding electrical resistivity once the optimization is performed with a non-null convergent behavior for Im [D(ε)]; (2) the contribution to itinerant holes is accounted for in D(ε), allowing to use the same approach to describe the dielectric function of semiconductors; (3) all parameters involved in the formulation of DF have known physical interpretation consistent with the role played in Equation (1); and (4) the number of parameters depends on the specific material and the spectral range being considered. The number of parameters is not selected under the criterion that it is the minimum requirement to access a minimum of the objective function described later. This number is selected from previous information available in the literature about conduction properties (electrons and/or holes), spectrophotometric measurements, energy loss spectra, and band structure calculations. These four features allow the present formulation to be applied even in the case of large spectral ranges and materials with significant spectral structure in the DF, as is the case of Ir.

Within the context of the optimization method described below, the following three substitutions are done in Equation (1): $\gamma_{oh} = \eta\gamma_{oe}$, $\Omega_{ph}^2 = \beta\chi\Omega_{pe}^2$, and $\varepsilon_{hf} = 1/f_o$ with $\beta = m_e/m_h$, $\chi = n_h/n_e = z_h/z_e$, and f_o with values between zero and unity. The counterparts of n_e and z_e are n_h and z_h for holes, respectively, with n_e different from n_h because Ir is a non-compensated metal [36]. A frequency-dependent relaxation time was assumed to improve the fitting of infrared optical properties of certain metals using the Drude model [37-39]. We assumed the same dependence on angular frequency for both electrons and holes: $1/\tau_e = 1/\tau_{oe} + \Lambda_e\omega^2$ and $1/\tau_h = 1/\tau_{oh} + \Lambda_h\omega^2$,

respectively. The corresponding scattering frequencies were $\gamma_e = \gamma_{oe}[1 + (\Omega/\Gamma_e)^2]$ and $\gamma_h = \gamma_{oh}[1 + (\Omega/\Gamma_h)^2]$, where Γ_e and Γ_h are two additional parameters to be optimized: $\Gamma_k = (h\gamma_{ok}/2\pi\Lambda_k)^{1/2}$ with the subscript letter $k = e$ for electrons, and $k = h$ for holes. These values for γ_e and γ_h substitute those of γ_{oe} and γ_{oh} in Equation (1), respectively. The seven parameters to be optimized in DF's Drude term [ε_D] are Ω_{pe}, γ_{oe}, β, χ, η, Γ_e, and Γ_h, which determine the contribution of conduction electrons and holes to the dielectric function of the metal. Additionally, the background polarization due to interband transitions beyond the spectral range considered is accounted for as the inverse of the optimized value of f_o. In $\sigma_o = \varepsilon_o\omega\varepsilon_2(\omega)$, when ω tends to zero, there are no interband transitions contribution in this limit.

The contribution of interband excitations to the dielectric function is approximated by the classical Lorentz summation term in Equation (1), where these excitations are modeled by resonance oscillators, each one associated with a j^{th} population of electrons bound to the metal ions whose resonance frequency (energy) is ω_j (Ω_j), i.e., $\varepsilon_L = \varepsilon_{L,1} + \varepsilon_{L,2} + \ldots + \varepsilon_{L,K}$ with $\varepsilon_{L,j}(\Omega) = f_j\Omega_{pe}^2/\{z_e[(\Omega_j^2 - \Omega^2) - i\Omega\gamma_j]\}$. The index j goes from 1 to K, with K equal to the number of oscillators considered. In quantum mechanics, the resonance frequencies correspond to electronic transitions between the occupied and vacant states close to critical points in the band structure. The resonance energies (Ω_j), Lorentzian widths (γ_j), and oscillator strengths (f_j) appear in the Lorentz term. The light absorption by bound electrons is determined by the imaginary component of the Lorentz term in the DF, which is proportional to $f_j\gamma_j$. The $N_p = 9 + 3K$ parameters in the DL model of the dielectric function are initially optimized using an Acceptance-Probability-Controlled Simulated Annealing (APCSA) approach [40, 41]. We implemented our APCSA code with certain improvements as described previously [33, 34]. In addition, we minimize the following merit function using the APCSA method

$$F = \frac{1}{2\kappa - N_p - 1}\sum_{i=1}^{\kappa}\left[\left(\frac{\varepsilon_1(\omega_i) - \bar{\varepsilon}_1(\omega_i)}{\bar{\varepsilon}_1(\omega_i)}\right)^2 + \left(\frac{\varepsilon_2(\omega_i) - \bar{\varepsilon}_2(\omega_i)}{\bar{\varepsilon}_2(\omega_i)}\right)^2\right], \quad (2)$$

where κ is the number of spectral points where the dielectric function's values are known, i.e., $\bar{\varepsilon}(\omega_i) = \bar{\varepsilon}_1(\omega_i) + i\bar{\varepsilon}_2(\omega_i)$. The number of degrees of freedom, i.e., the number of terms that can change in the minimization of F is 2κ minus the number of quantities that are being optimized, including F itself. This definition of the merit function allows us to simultaneously retrieve both $\varepsilon_1(\omega)$ and $\varepsilon_2(\omega)$ with minimal error throughout the spectral range considered. The optimizations were conducted until the solidification condition was satisfied: the lowest F-value for each temperature cycle was compared with the lowest values of the three preceding consecutive temperatures [40]. When the corresponding three relative differences are lower than the specified numerical tolerance Δ, the simulated annealing process is finished. We used $\Delta = 10^{-4}$. In the APCSA approach, the temperature is a control parameter with the same units the merit function has [42], which is updated from the dispersion in the merit function or accepted energy values once each cycle is finished. After this stage of optimization, the optimized values were used to repeat the process but with the application of an SPGM after each temperature cycle. We call this an SPGM-assisted APCSA approach applied to improve the solution. Details of the SPGM have been published elsewhere [43, 44]. The Appendix includes additional information on the components of the gradient of F obtained from the explicit expressions of ε_1 and ε_2.

Once the optimization is performed, a set of derived quantities were evaluated, as shown in Table 1, demonstrating the fundamental nature of the dielectric function to all extent. We assumed that

the holes contribute to the paramagnetic and diamagnetic susceptibilities in the same manner as by conduction electrons [45]. In the two-band model, Hall's coefficient listed in Table 1 was written as $R_H = -(1 - \chi q^2)/[ez_eN(1 + \chi q)^2]$ with $q = \beta/\eta$ [46].

Table 1 List of physical quantities evaluated once the optimization of the DL parameters is finished.

Number density of conduction electrons	$n_e = z_eN$
Number density of conduction holes	$n_h = z_hN = \chi n_e$
Average effective mass of conduction electrons	$m_e = n_e e^2/\varepsilon_o\omega_{pe}^2$
Average effective mass of holes	$m_h = m_e/\beta$
Intrinsic relaxation times [a]	$\tau_{ok} = h/2\pi\gamma_{ok}$
Fermi energies[a]	$E_k = h^2(3\pi^2n_k)^{2/3}/8\pi^2\, m_k$
Fermi velocities[a]	$v_k = (2E_k/m_k)^{1/2}$
Intrinsic mean free paths [a]	$L_k = v_k\tau_{ok}$
Densities of states at corresponding Fermi energies [a, b]	$\rho(E_k) = (3n_k/2E_k)V_{pc}$
Heat capacity coefficients [a, c]	$\gamma_{hcc,k} = \pi^2\, k_B^2\rho(E_k)/3$
Intrinsic charge-carriers mobilities [a]	$\mu_k = e\tau_{ok}/m_k$
Pauli's spin paramagnetic susceptibilities [a, d]	$\chi_k = \mu_o\mu_B^2\rho(E_k)$
Landau's diamagnetic susceptibilities [a, d] [47]	$\chi_k' = -(m/m_k)^2\chi_k/3$
Hall's coefficient	$R_H = -(n_e\mu_e^2-n_h\mu_h^2)/e(n_e\mu_e + n_h\mu_h)^2$
Static volume electrical conductivity	$\sigma_o = n_e e^2\tau_{oe}/m_e + n_h e^2\tau_{oh}/m_h$
Static volume resistivity	$\rho_o = 1/\sigma_o$
Thermal conductivity [e]	$\kappa_{th} = L\sigma_o T$
Effective number of Bohr's magnetons[f]	$p = (3\, k_B/\mu_o N_{av})^{½}(\chi_M T)^{½}/\mu_B$
Charge carriers coupling coefficient [g]	$\lambda = (\gamma_{exp}-\gamma_{hcc})/\gamma_{hcc}$

[a] $k = e$ for electrons and h for holes; [b] $V_{pc} = V_{cc}/4$ is the fcc primitive unit cell volume, and the densities of states is given in states/energy atom; [c] k_B is Boltzmann's constant, and the total heat capacity is given by $\gamma_{hcc} = \gamma_{hcc,e} + \gamma_{hcc,h}$; [d] m being the free electron mass, μ_B is the Bohr's magneton, μ_o is the free space magnetic permeability, and the total susceptibility is evaluated from $\chi_m = \chi_e + \chi_h + \chi_e' + \chi_h'$. [e] L is the Lorenz number and T is the absolute temperature. [f] Magnetic molar susceptibility is χ_M. [g] γ_{exp} is the experimental value of the heat capacity coefficient, with contributions from electron-electron and electron-phonon interactions.

Both electrons and holes contribute to the intrinsic conductivity in fractions given by $P_e = 1/[1 + \chi q]$ and $P_h = 1 - P_e$, respectively. In addition to the spectral dependence of $\varepsilon_2(\omega)$, the absorption of light was considered through the dynamic conductivity [$\sigma(\omega) = \varepsilon_o\omega\varepsilon_2(\omega)$] and the energy loss function as described in Section 6.

To compare with previous reports of Drude parameters, the added Drude dielectric susceptibilities corresponding to the second and third terms in the right side of Equation (1) [$\chi_{Drude} = -\Omega_{pe}^2/(\Omega(\Omega + i\gamma_e) - \Omega_{ph}^2/(\Omega(\Omega + i\gamma_h)]$ can be expressed approximately as $\chi_{eff} = -\Omega_o^2/[\Omega(\Omega + i\gamma_{eff})]$. The effective values of γ_{eff} are obtained from $\gamma_{eff} = -\Omega\cdot Im(\chi_{eff})/Re(\chi_{eff})$. As expected, this effective scattering frequency shows a dependence on energy that can be modeled by $\gamma_{eff} = \gamma_o(1 + (\Omega/\Gamma_o)^2)$, with regression coefficients close to unity. The fitting of γ_{eff} allows us to calculate both γ_o ($\tau_o = h/2\pi\gamma_o$)

and Γ_o. This approach to obtaining the γ_{eff}- and Γ_o-values holds when the Γ_e and Γ_h, as well as γ_{oe} and γ_{oh}, have similar orders of magnitude, i.e., when their ratios are about between unity and ten. Otherwise, the frequency-dependence of the effective scattering frequency must be fitted from some approximation of $\gamma_{eff} = [\gamma_e(\Omega^2 + \gamma_h^2) + \chi\gamma_h(\Omega^2 + \gamma_e^2)]/[(\Omega^2 + \gamma_h^2) + \chi(\Omega^2 + \gamma_e^2)]$ and depending on the orders of magnitudes of γ_{oe}/γ_{oh} and Γ_e/Γ_h. The value of effective volume plasma energy Ω_o was obtained for each spectral point from the relation $\Omega_o = [(-\mathrm{Re}(\chi_{eff}) + \mathrm{Im}(\chi_{eff}))\Omega^2(1 + \alpha^2)/(1 + \alpha)]^{1/2}$, with $\alpha = \gamma_{eff}/\Omega$, showing very low dispersion. Its average value was evaluated from the set of Ω_o values. The γ_o, Γ_o, and Ω_o parameters were considered as effective Drude quantities.

3. Band Structure Calculations Based on Density Functional Theory (DFT)

We have initially performed DFT calculations, with no inclusion of spin-orbit coupling (SOC), using a norm-conservative pseudopotential [48] and a dense *k*-point mesh for the band diagram and DOS spectra by solving the Kohn–Sham equation [49], with a plane wave basis set to calculate the band structure diagram (BSD), charge distribution and projected density of states (DOS) of Ir through the Quantum Espresso computational suite [50] (Figure 1). An exchange–correlation functional within the local density approximation was used as devised by Perdew, Becke, and Ernzerhof (PBE) [51, 52], using the Troullier–Martins procedure to generate norm-conserving pseudopotentials [53]. The norm-conservative pseudopotential was used with nine valence electrons per atom of Ir in the primitive unit cell. Unit cell relaxation provides us with a lattice constant of 0.389 nm, close to the experimental value of 0.384 nm [35, 54]. Thus, we showed the pertinence of the pseudopotential and exchange-correlation functional choice for our calculations.

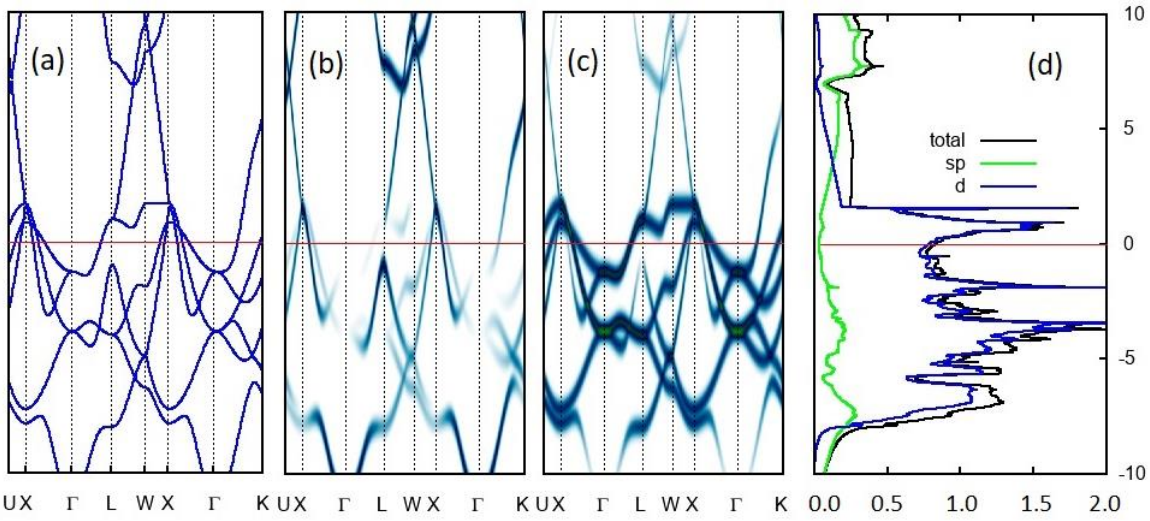

Figure 1 (a) Electronic band structure diagram (BSD) of Ir evaluated by DFT with no spin-orbit coupling. Projected DOS onto orthogonalized atomic orbitals resolved in momentum-space for (b) hybridized *sp*-orbitals, and (c) *d*-orbitals. (d) Total and projected DOS summed over all *k*-points. Values in the horizontal axis are given in states/eV atom. The vertical scale is given in eV, with the horizontal 0 energy indicating the standard Fermi level E_F (SFL).

The overestimation of the lattice constant is characterized by DFT-based methods using the PBE exchange-correlation functional [55]. The wavefunction cutoff was set to 1360 eV. The self-consistent calculation was achieved with an accuracy of 1.4×10^{-5} eV. We used the Methfessel–Paxton smearing function [56] to account for the metallicity of Ir, with a width of 0.272 eV and 10 × 10 × 10 mesh *k*-points to sample the Brillouin zone [57]. We used 500 *k*-points to obtain the BSD. Atomic positions were relaxed until the converged successive values of the pseudopotentials corresponded to relative differences lower than 10^{-4}. Figure 1(d) shows the DOS of Ir, as evaluated from DFT with no SOC. Similar spectral features have been reported by Noffke and Fritsche, who calculated the DOS at the Fermi level, $\rho(E_F)$, in about 1.04 states/eV atom (Figure 1 in [28]). Our evaluations provide around 0.84 states/eV atom with no spin-orbit coupling and 1.06 states/eV atom when the spin-orbit is considered (Figure 2). The values 0.91 and 1.01 states/eV atom have been reported for $\rho(E_F)$ [29, 31]. The DOS is predominantly determined by the contribution of *d*-states (Figure 1(c)), with the Fermi energy just below the largest peak of the DOS at energies above the standard Fermi level (SFL). The width for the *d*-band was close to 10.6 eV, i.e., the *d*-band extended from about 8.9 eV below the Fermi level to 1.7 eV above. The SFL, with respect to the bottom of the hybridized *sp* band, was around E_F = 10 eV. A heavy *d*-hole-like sheet extending from the W- to the X- symmetry point, at energies between 1.29 and 1.41 eV above the SFL, and light *d*-hole-like pockets centered around the X-point, at 0.52 and 0.92 eV above the Fermi level, are displayed in the BSD of Figure 1(a) and Figure 1(c). A similar finding has been reported for Pd [58]. Another band of empty *d*-states just above the Fermi level was displayed in the L-W direction with energies between 0.42 and 1.29 eV. The presence of these *d*-hole states correlated with peaks in the projected density of *d*-states, centered at 0.16 and 1.38 eV just above the SFL, whose maximum values are 0.91 and 0.93 states/eV atom when j = 5/2, respectively, 0.51 and 0.34 states/eV atom when j = 3/2, respectively.

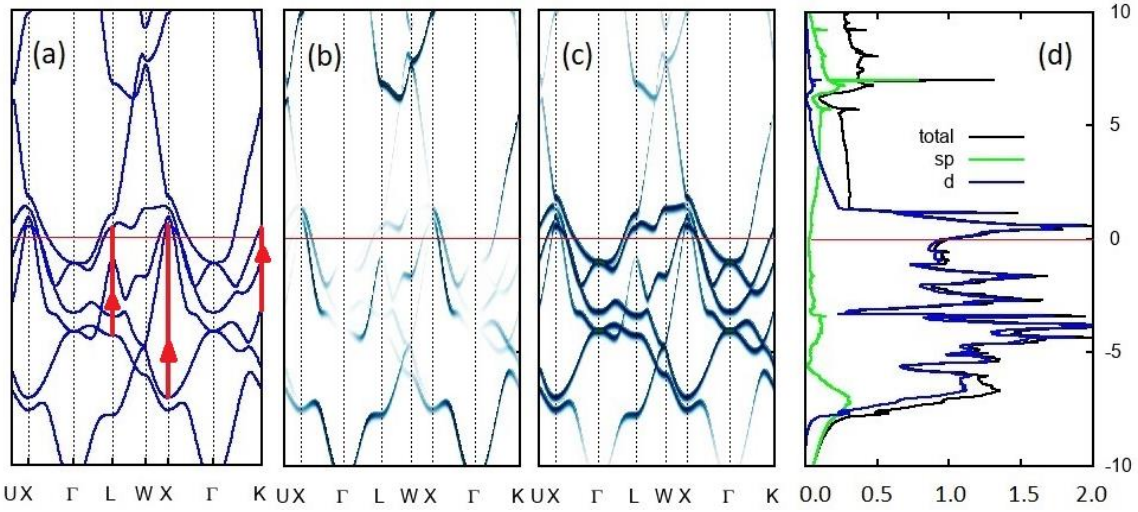

Figure 2 (a) Electronic BSD of Ir evaluated by DFT with the inclusion of spin-orbit coupling. Projected DOS onto orthogonalized atomic orbitals resolved in momentum-space for (b) hybridized *sp*-orbitals and (c) *d*-orbitals. (d) Total and projected DOS summed over all *k*-points. The values in the horizontal axis are given in states/eV atom. The vertical scale is given in eV, with the horizontal 0 energy indicating the standard Fermi level. The red arrows in the left figure are indicated for use in the discussion.

Itinerant *s*- or *sp*-electrons contribute to the electrical conduction in Ir undergoing transitions up to empty *d*-states of neighboring atoms, just above E_F. The three red arrows in Figure 2(a) indicate the plausible transitions of these electrons. This issue is discussed in detail in Section 5. The inclusion of SOC in DFT calculations leads to a more structured DOS, as seen in Figure 2(d). Regarding the BSD, the major change is the splitting of the *d*-band displayed in the Γ-L direction, which crosses the SFL. At the Γ-symmetry point, the lower *d*-band displayed in the energy range showed a splitting due to the SOC, which projected toward the Γ-Δ and Γ-L-W directions.

Once the SPGM–APCSA optimization is achieved, the density of states and Fermi energies for itinerant conduction holes and electrons as derived parameters were used and compared these quantum mechanics parameters with corresponding ones were obtained from the BSD. Thus, we will be able to distinguish the transitions involved in the transport of itinerant charge carriers.

4. Dielectric Function of Bulk Iridium

The DF of Ir was obtained by Weaver et al. for a large specular polycrystalline sample normally illuminated [19] (read lines in Figure 3(a)). The purity of the sample was unspecified. The spectral absorptivity measurements (A) at low temperature (4.2 K) were used to obtain the reflectivity spectrum (R = 1 - A) in the energy range of 0.2 to 4.4 eV, and it was directly measured at RT in the energy range of 3.0 to 40 eV. A unique reflectivity spectrum was considered in the spectral range of 0.20 to 40 eV, with good agreement in the region of the overlap of the two reflectivity spectra previously measured. The Kramers–Kronig analysis was used to obtain the DF from inversion of the reflectivity spectrum [20]. The analysis by Weaver et al. includes a report of the spectral dependence of the dynamic conductivity, which is proportional to $\bar{\varepsilon}_2$, the imaginary part of the retrieved DF (blue line in Figure 3(b)). The following resonance energies, reported in eV, are: Ω_2 = 1.05, Ω_3 = 1.9, Ω_4 = 3.1, Ω_5 = 4.12 [19]. In the same study, the imaginary component of the DF shows two additional higher resonance energies at Ω_6 = 10.8 and Ω_7 = 18.8 eV. Finally, the experimental energy loss function, -Im $[1/\bar{\varepsilon}(\omega)]$, depicts a resonance energy at Ω_8 = 33 eV. These authors comment about a low energy resonance in Ω_1 = 0.40 eV reported in [17].

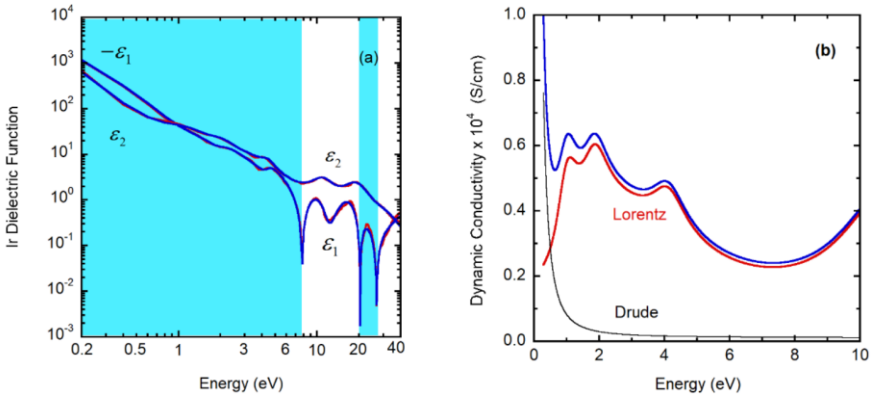

Figure 3 (a) RT real (ε_1) and imaginary (ε_2) components of the DF of Ir as fitted from an SPGM-assisted APCSA optimization with eight resonance energies in the Lorentz term (blue lines). Red lines are traced from the experimental values of the DF [20]. Values of ε_1 are negative in the bluish spectral ranges. (b) Spectral dependence of the dynamic conductivity, with contributions from charge–carriers (Drude) and interband transitions (Lorentz).

The APCSA optimization was performed by assuming small variations in the energy resonances around the set of indicated Ω_j-values, with $\kappa = 200$ spectral points and $K = 8$ resonance energies. The specified number of spectral points was generated by cubic spline interpolation from the 124 data reported previously [20]. The other parameters were optimized by searching in ranges with mobile boundaries, requiring 106 temperature cycles to satisfy the solidification condition. At the end of the first stage of the APCSA optimization, the value of the merit function was $F = 0.027$. With the application of the SPGM-assisted APCSA strategy, the final merit function reached the value $F = 0.010$.

4.1 Optimized Transport Parameters

The modeling of the DF was displayed in Figure 3(a), with optimized values of the parameters specified in Table 2 and derived quantities in Table 3. Figure 3(b) shows the spectral dependence of the dynamic conductivity, with contributions from the Lorentz (interband transitions) and Drude (charge-carriers transport) terms to the imaginary component of the DF, whose spectral details resemble those reported in [19] for the total conductivity. The optimized f_o-value close to unity implies that the contribution to the dielectric function by interband transitions beyond 40 eV was small ($\varepsilon_{hf} = 1.06$), i.e., there existed a small background polarization associated with interband transitions at energies beyond the spectral range considered.

Table 2 SPGM-assisted APCSA optimized DL parameters used to calculate the RT dielectric function of a polycrystalline annealed bulk sample of Ir [20]. Parameters are given in eV, except the dimensionless z_e, β, η, χ, f_o, and the oscillator strength f_j-values. Values in bold correspond to Drude parameters, the rest are the Lorentz parameters, and F is the optimized value of the merit function.

Parameter	Value	Parameter	Value
Ω_{pe}	**4.464**	f_4	1.755
f_o	**0.944**	γ_4	4.777
γ_{oe}	**0.095**	Ω_4	3.218
B	**2.674**	f_5	0.202
H	**0.987**	γ_5	1.193
X	**0.760**	Ω_5	4.381
Γ_e	**3.648**	f_6	1.961
Γ_h	**3.600**	γ_6	5.143
f_1	0.301	Ω_6	11.10
γ_1	1.268	f_7	6.031
Ω_1	0.424	γ_7	9.415
f_2	0.556	Ω_7	19.43
γ_2	1.311	f_8	3.250
Ω_2	1.210	γ_8	20.41
f_3	0.186	Ω_8	31.17
γ_3	0.917	z_e	0.333
Ω_3	2.066	F	0.010

Table 3 Set of derived quantities for the Ir bulk sample whose room temperature DF is depicted in Figure 3(a) with the optimized DL parameters reported in Table 2. Quantities in bold are the effective Drude parameters.

Parameter	Value	Parameter	Value
γ_o (eV)	**0.09**	κ_{th} (W/mK)	67.3
Γ_o (eV)	**3.62**	E_e (eV)	1.84
Ω_o (eV)	**7.77**	E_h (eV)	4.09
τ_o (fs)	**7.00**	$\rho_e(E_e)$ (states/eV atom)	0.27
γ_{oh} (eV)	0.09	$\rho_h(E_h)$ (states/eV atom)	0.09
ε_{hf}	1.06	$\gamma_{hcc,e}$ (mJ/K^2 mol)	1.28
z_h	0.25	$\gamma_{hcc,h}$ (mJ/K^2 mol)	0.44
τ_{oe} (fs)	6.93	γ_{hcc} (mJ/K^2 mol)	1.72
τ_{oh} (fs)	7.02	L_e (nm)	4.35
Λ_e (as)	4.70	L_h (nm)	10.8
Λ_h (as)	4.80	R_H (m^3/As)	12.9×10^{-11}
m_e/m	1.64	v_e (m/s)	0.63×10^6
m_h/m	0.61	v_h (m/s)	1.53×10^6
μ_e (cm^2/Vs)	7.45	χ_e (cm^3/g)	0.57×10^{-6}
μ_h (cm^2/Vs)	20.2	χ_h (cm^3/g)	0.20×10^{-6}
ρ_o (μΩ cm)	11.6	χ_e' (cm^3/g)	-0.07×10^{-6}
P_e (%)	32.7	χ_h' (cm^3/g)	-0.17×10^{-6}
P_h (%)	67.3	χ_m (cm^3/g)	0.53×10^{-6}
σ_o (S/cm)	8.63×10^4	n_e (electrons/cm^3)	2.37×10^{22}
σ_e (S/cm)	2.82×10^4	n_h (electrons/cm^3)	1.80×10^{22}
σ_h (S/cm)	5.81×10^4	λ	0.32
		p	0.12

The β-value was close to 8/3, meaning that the average effective mass of conduction electrons was larger than that of the holes (m_e = 1.64 m and m_h = 0.61 m). Similar values of the scattering frequencies of conduction electrons and holes were obtained according to the value close to unity for the η-parameter. Scattering frequencies, $\gamma_{oe,}$ and γ_{oh}, were determined by electron-electron and hole-hole interactions, respectively, as well as interactions of charge carriers with phonons. According to the optimized values of Γ_e and Γ_h, the frequency dependence of the relaxation times was negligible (Λ_e = 4.70 and Λ_h = 4.80 as). This is expected when considering the annealing process applied to the sample used by Weaver et al. [19]. The number density of electrons was larger than that of holes (χ = 0.76), with z_e = 0.33. A similar value was reported for Pd, a transition metal characterized by z_e = 0.36 [59]. Similar values were reported for other transition metals: 0.38 for Ti, 0.40 for Zr, and 0.44 for Hf [60].

After subtracting the residual contribution, the experimental resistivity values of Ir (ρ_{exp}) were reported between 0.005 μΩ cm at low temperatures and 5.0 μΩ cm at room temperature [61]. The value obtained as a quantity derived from the optimization process (ρ_o = 11.6 μΩ cm) agreed with the order of magnitude for the corresponding static conductivity as extrapolated from the spectral dependence of the dynamic conductivity reported by Weaver et al. [19]. Observation $\rho_o > \rho_{exp}$

suggests the presence of impurities in the sample prepared by Weaver et al. The Hall's coefficient (R_H = 12.9 × 10^{-11} m^3/As) is larger than the values reported for samples at low- and room-temperatures, namely, 3.49 × 10^{-11} m^3/As at 81 K and 3.18 × 10^{-11} m^3/As at 300 K, respectively [62]. These two parameters, ρ_o and R_H, are sensitive to the purity of the sample. The effect of impurities is used in evaluating the parameters through the intrinsic relaxation times of charge carriers. The thermal conductivity appears to be affected by impurities. Its derived value, κ_{th} = 67.3 W/mK at T = 300 K, was evaluated using the Lorenz number reported for Ir: L = 2.60 × 10^{-8} WΩ/K^2 [63]. The reported value in the literature is around 150 W/mK [64].

The large values of resistivity and Hall's coefficient, as compared with the reported data, indicate a significant content of impurities in the sample used by Weaver et al. In addition, the light diffusively reflected by the surface of the sample corresponds to the absorption by the medium when normalizing reflectivity measurements. Although the number density of holes (z_h = 0.25) is less, they primarily contribute to the conduction in Ir, as shown by σ_e and σ_h values (P_e = 33% and P_h = 67%). The relative effective mass of holes was determined by Hörnfeldt et al. using de Haas-van Alphen oscillation measurements [65], with values between 0.23 and 1.28 depending on the crystallographic plane and specific hole pocket considered. Our calculated average value (m_h/m = 0.61) was within this range. Grodski and Dixon have reported values for the relative effective mass between 1.34 and 3.02 for conduction electrons with states in the Γ-point [66]. In addition, the average value calculated from the optimization process (m_e/m = 1.64) is within this range.

In addition to the effect of impurities and surface roughness, there is another aspect that significantly influences the values of the transport parameters. For example, thermal conductivity value, which is proportional to the electrical conductivity, is sensitive to the limiting behavior of the imaginary component of the DF when the frequency tends to zero. At low energies, the dielectric function was obtained from absorptivity measurements recorded at low temperatures. From the visible to the ultraviolet, measurements were recorded at RT. The net effect of these three factors was reflected in a thermal conductivity derived from the optimization whose value is around 50% lower than the measurements reported in the literature.

4.2 Magnetic Susceptibility and Enhancement by Charge Carrier Exchange Correlation

The reported magnetic susceptibility of Ir is χ_{exp} = 0.133 × 10^{-6} cm^3/g at room temperature [67]. A higher value is expected at low temperatures, which is consistent with our calculation derived from the SPGM-assisted APCSA optimization: χ_m = 0.53 × 10^{-6} cm^3/g. The total molar susceptibility is obtained from the total mass susceptibility as follows: $\chi_M = M\chi_m$ = 1.02 × 10^{-4} cm^3/mol, with M = 192.217 g/mol as the atomic weight of Ir, and a similar relation for the diamagnetic susceptibilities. The fact that χ_m > 0.133 × 10^{-6} cm^3/g (the experimental value) is an indication of the presence of traces of ferromagnetic elements in the sample studied by Weaver et al. This also affects the enhancement of the magnetic susceptibility due to electron–phonon interactions. According to Curie's law for paramagnetic materials and the relation between diamagnetic and paramagnetic susceptibilities, the number of effective Bohr magnetons is given by $p = (3\, k_B/\mu_o N_{av})^{½}(\chi_M T)^{½}/\mu_B$ with N_{av} as Avogadro's number. The average magnetic moment per atom is $\mu_{avg} = p\mu_B$. The evaluation for Ir results in p = 0.10 at room temperature. If the exchange–correlation effect is included, $\chi_{M,ec} = \chi_M/[1-\rho(E_F)I_F]$ where I_F is the exchange–correlation integral and $\rho(E_F)I_F$ is the Stoner parameter [68,

69]. For Ir, I_F has been reported by Sigalas et al. as 0.287 eV, and with $\rho(E_F)$ = 1.01 states/eV atom [31], the evaluations results in $\chi_{M,ec}$ = 1.44 × 10^{-4} cm^3/mol and p = 0.12.

The electrical conduction is attributed to itinerant electrons and holes charge carriers, implying that these charge carriers partially behave like free charge carriers or like localized ones. The presence of this partial localization or its spatial confinement decreases the magnetic susceptibility, as shown by Cahaya, who extended the known relations of Pauli and Landau susceptibilities by incorporating the following two facts in his derivation [70]: (a) by considering an infinite quantum well, he assumed null values of the charge carrier wave functions at the boundaries of the medium instead of periodic boundary conditions, and (b) an artificial local confinement was introduced through a spatially periodic magnetic field whose spatial period λ_q was tuned through the wavenumber $q = 2\pi/\lambda_q$. This field introduced local confinement of charge carriers in those planes perpendicular to the direction of the magnetic field. He obtained the same expression for Pauli and Landau magnetic susceptibilities, times corresponding factors given by

$$Z_{P,k} = \frac{1}{2} + \frac{1 - x_k^2}{4x_k} ln \left| \frac{x_k + 1}{x_k - 1} \right|, \tag{3a}$$

$$Z_{L,k} = \frac{3}{8x_k^2} \left[1 + x_k^2 - \frac{(1 - x_k^2)^2}{2x_k} ln \left| \frac{x_k + 1}{x_k - 1} \right| \right] = \frac{3}{4x_k^2} \left[1 - (1 - x_k^2) Z_{P,k} \right], \tag{3b}$$

where $x_k = q/2k_{F,k}$, with $k_{F,k}$ as the Fermi momentum of the k^{th} charge carrier type. These two parameters tend to unity when q tends to zero, i.e., the known expressions of paramagnetic and diamagnetic susceptibilities are recovered as the local confinement disappears. Otherwise, the values of Z_P and Z_L are lower than unity, i.e., they are diminution factors, $Z_{P,k}$ being the Lindhard function [71]. In the absence of an external magnetic field, other effects contribute to a spatially periodic or quasi-periodic internal magnetic field: thermal fluctuations of atomic nuclei around their equilibrium positions [72] and small variations in the quasi-stationary electrostatic screening potential due to thermal fluctuations in the position of the center of mass of the electronic gas of charge carriers [73].

To apply Cahaya's formalism linked to the initially calculated magnetic Pauli and Landau susceptibility components for both electrons and holes, we wrote the corresponding mean free paths in terms of the spatial period of the magnetic field: $L_k = N_{P/L,k}\lambda_{q,P/Z,k}$ and x_k becomes $x_k = \pi N_{P/L,k}/L_k k_{F,k}$ with $k_{F,k} = (3\pi^2 n_k)^{1/3}$ [$k_{F,e}$ = 8.89 nm, $k_{F,h}$ = 8.11 nm]. Table 4 shows the results. The fraction of each contribution to the total susceptibility ($F_{P,k}$ and $F_{L,k}$ with k = e and h) is calculated from the results of the optimization, after applying the enhancement due to exchange correlations.

Table 4 Diminution factors for both conduction electrons and holes contributing to the Pauli and Landau magnetic susceptibilities. The lattice constant is a = 0.389 nm.

Electrons (L_e/a = 4.790)				Holes (L_h/a = 59.21)			
Pauli		Landau		Pauli		Landau	
$N_{P,e}$	17.83	$N_{L,e}$	28.59	$N_{P,h}$	40.38	$N_{L,h}$	64.76
$Z_{P,e}$	0.178	$Z_{L,e}$	0.178	$Z_{P,h}$	0.178	$Z_{L,h}$	0.178
$\lambda_{q,P,e}$	0.244	$\lambda_{q,L,e}$ (nm)	0.152	$\lambda_{q,P,h}$ (nm)	0.267	$\lambda_{q,L,h}$ (nm)	0.167
$\lambda_{q,P,e}/a$	0.627	$\lambda_{q,L,e}/a$	0.391	$\lambda_{q,P,e}/a$	0.688	$\lambda_{q,P,e}/a$	0.429

The four contributions giving the measured susceptibility are evaluated by assuming that the same fractions can be associated with the reported experimental values. For each component, the equation $|F_{P/L,k}\cdot\chi_{exp} - Z_{P/L,k}\cdot\chi_k| = \varepsilon$, with ε close to or lower than 10^{-10}, has been solved for $\chi_1 = \chi_{e,ec}$, $\chi_2 = \chi_{h,ec}$, $\chi_3 = \chi_{e,ec}'$, and $\chi_4 = \chi_{h,ec}'$.

4.3 Charge-Carrier Heat Capacity and the Coupling Constant

The reported value of the charge–carrier heat capacity coefficient is γ_{exp} = 3.14 mJ/K^2 mol [74], which includes the contributions from electron-phonon coupling (EPC), and exchange correlation (EC) between charge carriers. The value obtained from the optimization process was significantly lower, γ_{hcc} = 1.72 mJ/K^2 mol, about half of the reported one, implying that the contributions from the EPC and EC are large in Ir (see Table 4 in [64]). The total heat capacity coefficient γ, is given by the relation $\gamma = \pi^2 k_B^2 \rho(E_F)(1 + \lambda)/3$ [75] with contributions from charge carriers and electron-phonon interactions. From $\gamma = \gamma_{exp} = \gamma_{hcc}(1 + \lambda)$ with λ as the coupling strength of the charge carriers both to the lattice phonons and to other charge carriers [76], $\lambda = (\gamma_{exp}-\gamma_{hcc})/\gamma_{hcc} = 0.83$ is obtained.

These evaluations do not account for the effect of EC between charge carriers at the Fermi surface neither EPC in the value of γ_{hcc} obtained from the optimization. McMillan estimated λ for Ir as 0.34 [75]. The electronic specific heat is given by $C = \gamma T$, where T is the absolute temperature, and γ is the specific heat coefficient, which can also be represented as $\gamma = (\pi k_B)^2 nm/(h k_F/2\pi),^2$ where $k_F = (3\pi^2 n)^{1/3}$ is the Fermi momentum, n is the number density of charge carriers, and m is the effective mass of each one. If the previous equation for γ is applied to an ideal electron gas, with no interactions between charge carriers or between them and the phonons, $\gamma \rightarrow \gamma_{o,k} = (\pi k_B)^2 n_k m/(h k_{F,k}/2\pi)^2$ with $k = e$ or h. In the context of the present optimization approach, $\gamma_k = (\pi k_B)^2 n_k m_k/(h k_{F,k}/2\pi)^2$. Consequently, $\gamma_k/\gamma_{o,k} = m_k/m$. This relation is valid in the limit of T→0, where the Fermi momentum remains unchanged by many-body effects according to the Luttinger theorem [77, 78]. The optimized values of relative effective masses of electrons and holes become enhancement ($\lambda_k > 0$) or diminution ($\lambda_k < 0$) factors [$m_k/m \equiv 1 + \lambda_k$] that must be applied to the first estimations of the corresponding specific heat coefficients. The corrected values are $\gamma_{hcc,e}\rightarrow(1 + \lambda_e)\cdot\gamma_{hcc,e}$ = 2.10 mJ/K^2 mol and $\gamma_{hcc,h}\rightarrow(1 + \lambda_h)\cdot\gamma_{hcc,h}$ = 0.27 mJ/K^2 mol. The recalculated total heat capacity coefficient is γ_{hcc} = 2.37 mJ/K^2 mol. The evaluation of Papaconstantopoulos, based on tight-binding calculations, results in 2.20 mJ/K^2 mol [79]. The corrected value of the electron-phonon coupling parameter is λ = 0.32, which is close to that reported by McMillan [75].

4.4 Optimized Interband Energy Resonances

The optimized values of resonance energies associated with interband transitions are close to those initially used as restricted values in the first APCSA optimization. Once the second stage of optimization was performed, Ω_1 changes from 0.40 to 0.42 eV with a 5% variation with respect to the initial value [Ω_1: 0.40→0.42 (5%)]. For other resonances, the following variations existed: Ω_2: 1.05→1.21 (15%); Ω_3: 1.90→2.07 (9%); Ω_4: 3.10→3.22 (4%); Ω_5: 4.12→4.38 (6%); Ω_6: 10.8→11.1 (3%); Ω_7: 18.8→19.4 (3%); and Ω_8: 33.0→31.2 (5%). These optimized resonance energies must be considered effective because each one could correspond to convolution of several sets of transitions between bands, with similar energy gaps between initial and final bands. We will again consider these resonance energy values when calculating the densities of states of final states involved in these transitions, according to the formulation given in Section 8.

5. Densities of States and Fermi Energies of Conduction Holes and Electrons

The values of the density of states of itinerant conduction electrons and the corresponding Fermi energy, derived from the SPGM-assisted APCSA optimization, are $\rho(E_e)$ = 0.27 states/eV atom and E_e = 1.84 eV, respectively. These values can be approached from the band structure diagram in the following manner: the contribution to electrical conduction in metal transitions is associated with electrons transitioning from *s*- to *d*-bands [80]. Figure 4(a) depicts a zoomed image of the density of states displayed in Figure 2(d) and shows in detail the density of states of *s*-electrons below the SFL. The composition of this *s*-DOS is highlighted with number labels for the nine peaks displayed. Each j^{th} peak can be modeled as a Gaussian function of amplitude H_j and deviation σ_j. The composition of the fourth peak has not been resolved. It will be considered as a single peak in the following analysis. The area of each peak was $A_j = (2\pi)^{1/2}\sigma_j H_j$. Each σ_j-value was obtained from that point where the height of the peak decreased to the value $H_j e^{-1/2}$. The areas obtained are used to calculate the weighted average for the density of states and the Fermi energy. Those transitions corresponding to the largest peaks closer to the SFL contribute more significantly to these averages.

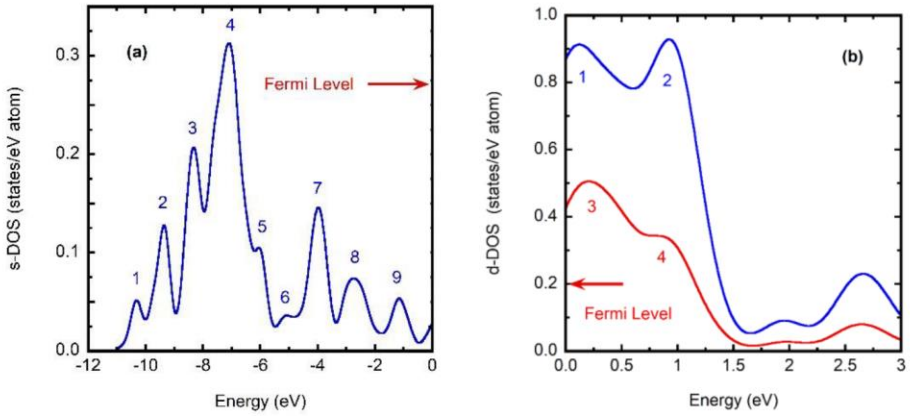

Figure 4 (a) DOS below the standard Fermi level for *s*-states whose composition has been highlighted with number labels for nine peaks displayed. (b) DOS above the standard Fermi level for *d*-states (blue and red colors for j = 5/2 and j = 3/2, respectively). The four peaks initially considered in the analysis are numbered.

Therefore, we considered the third, fourth, and seventh peaks with the following values: σ_3 = 0.29, σ_4 = 0.42, and σ_7 = 0.30 eV; H_3 = 0.21, H_4 = 0.31, and H_7 = 0.15 eV^{-1}. The areas are A_3 = 0.15, A_4 = 0.33, and A_7 = 0.11. The weighted average value of the DOS of these itinerant conduction electrons was $\langle\rho(E_e)\rangle = (A_3H_3 + A_4H_4 + A_7H_7)/(A_3 + A_4 + A_7)$ = 0.25 states/eV atom. The average Fermi energy is $\langle E_e\rangle = N_\sigma(A_3\sigma_3 + A_4\sigma_4 + A_7\sigma_7)/(A_3 + A_4 + A_7)$ = 1.82 eV with N_σ = 5 in this case. Given the position on the energy of each peak, E_j, the weighted average of the Fermi energy was calculated from the energy range around each peak, which was approximated from $E_j - N_\sigma\sigma_j/2$ to $E_j + N_\sigma\sigma_j/2$. This explains the factor N_σ used to evaluate the average Fermi energy. The drawback of this method was the use of N_σ as a fitting parameter. When its value was close to 3, it would be interpreted as an indication of the presence of a Gaussian peak. When N_σ takes a value close to 10, it implies that the tails of the peak decrease more slowly than those of Gaussian profiles. In this case, a Lorentzian behavior is expected for energies lower than $E_j - \sigma_j$ and larger than $E_j + \sigma_j$. Another method to interpret the information provided by the band structure diagram is to consider only the dominant peak. In this

case, A_4 = 0.33 is equal to the average number of electrons per atom participating in the transitions as itinerant charge carriers. With $<\rho(E_e)>\Delta E_4 = A_4$, one has that $<\rho(E_e)> = A_4/N_\sigma\sigma_4$ = 0.26 states/eV atom with N_σ = 3. The corresponding Fermi energy can be obtained from $<E_e> = 3A_4/[2<\rho(E_e)>]$ = 1.90 eV. These weighted averages are close to those obtained from the APCSA optimization. The correlation between these three peaks considered and the band structure diagram shown in Figure 4(a) can be used to discriminate the transitions involved. The third peak correlated to the transitions at the Σ-point, between the two parallel bands: from 7.77 eV below to that standard Fermi level (see the right red arrow in Figure 2(a)). The dominant fourth peak was contributed by transitions from the same parallel bands; however, it also included transitions at the X-symmetry point, from the band 6.97 eV below the Fermi level up to empty states of the *d*-hole pockets (see the red arrow in the middle of Figure 2(a)). The seventh peak was determined by transitions close to the K-symmetry point, from 3.90 eV below the Fermi level up to the parallel band just above the SFL (see the left red arrow in Figure 2(a)).

For conduction holes, the derived values of the density of states and the corresponding Fermi energy are $\rho(E_h)$ = 0.09 states/eV atom and E_h = 4.09 eV, respectively. The contribution of these charge carriers to conduction is attributed to intra-band transitions in the *d*-band, just above the Fermi level and involving the *d*-hole pockets and/or the *d*-hole sheet mentioned in Section 3. Figure 4(b) shows the *d*-DOS for two values of the quantum number j associated with the spin-orbit coupling (j = 3/2 and 5/2). In addition, we numbered those peaks as well resolved: the first two peaks correspond to the *d*-band with j = 5/2, and the other two peaks are displayed for the *d*-band with j = 3/2. After analyzing the contributions of each peak to the average density of states and the average number of holes participating in the intra-band transitions, the only alternative that approached the values obtained from the APCSA optimization corresponded to the fourth peak characterized by H_4 = 0.34 states/eV atom and σ_4 = 0.27 eV. The corresponding area is A_4 = 0.23 andthe average density of states is $<\rho(E_h)> = A_4/N_\sigma\sigma_4$ = 0.085 states/eV atom with N_σ = 10. The large value of N_σ could be attributed to a Lorentzian characteristic of this peak. The average Fermi energy is $<E_h> = 3A_4/[2<\rho(E_h)>]$ = 4.06 eV. The agreement with those values obtained from the SPGM-assisted APCSA optimization was satisfactory. The dominant intra-band *d*-hole transitions correlated with the fourth peak were those involving the *d*-hole-like sheet shown between X- and W-symmetry points, at about 1.30 eV above the SFL, toward the *d*-band displayed between the W- and L-symmetry points.

6. Bulk and Surface Energy Loss Functions

The bulk electron energy loss function can be written in the form $L^{(B)}(\Omega) = -Im[\,1/\varepsilon(\Omega)] = -A_o^{(B)}(\Omega)\,Im[\,1/\varepsilon_D(\Omega)] - B_o^{(B)}(\Omega)\,\mathrm{Im}[\,1/\varepsilon_L(\Omega)]$, with ε_D and ε_L as the Drude and Lorentz contributions, respectively [81, 82]. In this way, $L_D^{(B)}(\Omega) = -A_o^{(B)}(\Omega)\,\mathrm{Im}[\,1/\varepsilon_D(\Omega)]$ and $L_L^{(B)}(\Omega) = -B_o^{(B)}\,\mathrm{Im}[\,1/\varepsilon_L(\Omega)]$ are the bulk ELFs corresponding to the charge-carriers and bound electrons, respectively. The real values of $A_o^{(B)}$ and $B_o^{(B)}$ coefficients are obtained at each Ω-point by solving the previous equality for $Im[\,1/\varepsilon(\Omega)]$ along with that for the real component $\{\mathrm{Re}[\,1/\varepsilon(\Omega)] = A_o^{(B)}(\Omega)\,\mathrm{Re}[\,1/\varepsilon_D(\Omega)] + B_o^{(B)}(\Omega)\,\mathrm{Re}[\,1/\varepsilon_L(\Omega)]\}$. This allows a system of two equations with two unknowns at each spectral point. A similar approach is followed to perform the decomposition of the surface ELF: $L^{(S)}(\Omega) = -\,\mathrm{Im}\{\,1/[\varepsilon(\Omega)+1]\}$ in terms of $L_D^{(S)}(\Omega) = -A_o^{(S)}(\Omega)\,\mathrm{Im}\{\,1/[\varepsilon_D(\Omega)+1]\}$ and $L_L^{(S)}(\Omega) = -B_o^{(S)}(\Omega)\,\mathrm{Im}\{\,1/[\varepsilon_L(\Omega)+1]\}$ [83]. Figure 5(a) displays the results for the bulk

ELF values, and Figure 5(b) corresponds to the surface ELF spectra. Based on the total bulk and surface ELF spectra, Weaver et al. assigned the low-energy peaks to excitations of volume and surface plasmons spectrally located at 7.8 and 7.2 eV, respectively [19]. From our deconvolution, the corresponding resonance energies of these plasmons were calculated to be 7.6 and 7.0 eV (see bold labels **1** in Figure 5). From the SPGM-assisted APCSA, the effective volume plasmon energy corresponding to its resonance frequency was calculated as Ω_o = 7.7 eV. Other two couples of volume- and surface-plasmons are displayed: the first at 14.0 and 13.3 eV (see bold labels **2**) and the second at 36.4 and 26.2 eV (see bold labels **3**). In addition, Weaver et al. interpreted that the largest peak of the total bulk ELF was due to the superposition of a plasmon excitation and absorption due to interband transitions. Recently measured ELF of Ir showed absorption peaks at 8.9, 15.4, and 31.0 eV, with the other two peaks at 54.2 and 67.0 eV [24]. The decomposition performed showed the spectral superposition of both plasmon excitations and electronic transitions. It is difficult to distinguish the true characteristic of the peaks just from the total ELF spectra, as stated by Weaver et al. Additional low-energy volume and surface plasmons are displayed at energies of 1.3 and 0.8 eV, respectively. These oscillations are probably attributed to the hybridization of collective excitations of bound electrons participating in interband transitions that accounted for the first three oscillators. In addition, a surface plasmon was obtained at 3.9 eV. Its corresponding volume counterpart was not resolved due to the superposition with the tail of the volume excitation **1** at energies lower than 7.6 eV.

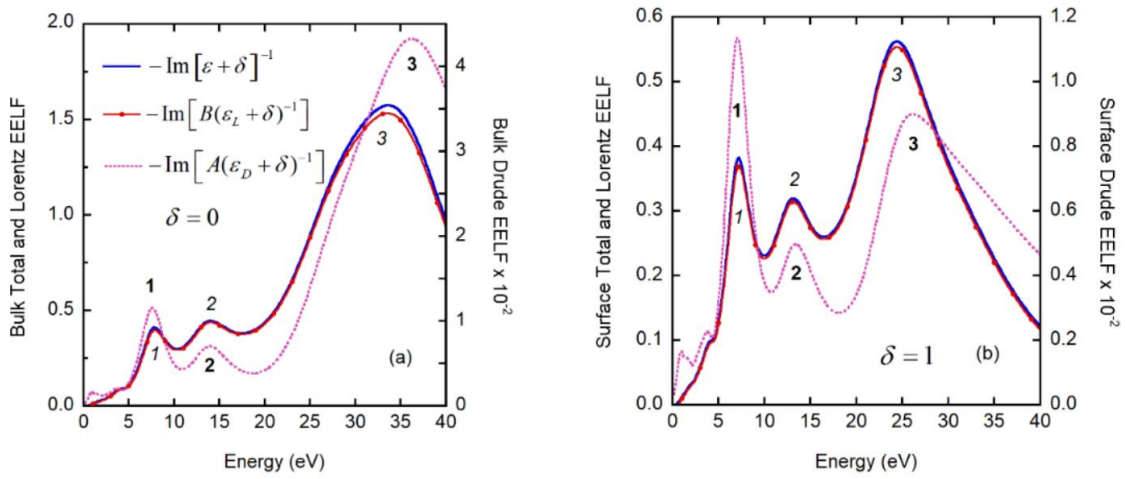

Figure 5 Bulk (a) and surface (b) energy loss function (ELF) for the Ir sample whose modeled DF is displayed in Figure 3(a). The subscripts D and L are used to specify the ELF for the charge-carriers (Drude) and bound electrons (Lorentz). Each spectrum is dominated by the presence of three peaks, as indicated by the labels of the figures.

Bound electrons related to the fourth and fifth oscillators could be involved in the collective oscillations and correlated with these low-energy peaks of the bulk and surface ELFs. The low-energy structure in the ELF of Ir was slightly observed from the analysis reported in [84], with the predominant peaks at 7.9, 14.8, and 32.2 eV.

7. Effective Numbers of Electrons and Densities of States

Considering the bulk ELF, the effective total number of bulk electrons and holes per atom participating as charge carriers and bound electrons per atom involved in interband transitions in the spectral range considered can be evaluated from the partial sum rule [85]

$$Z_{eff} = \frac{2}{\pi\Omega_{pe}^2}\int_0^{\Omega_{\max}} \Omega \cdot \mathrm{Im}[-\frac{1}{\varepsilon(\Omega)}]d\Omega = \frac{2}{\pi\Omega_{pe}^2}\int_0^{\Omega_{\max}} \Omega \cdot L^{(B)}(\Omega)d\Omega, \quad (4)$$

with Ω_{max} = 40 eV in our case. The integration is performed with the Simpson rule and Richardson extrapolation [86]. The optimized parametric form of the DF is used to extrapolate $L^{(B)}(\Omega)$ from Ω_{min} = 0.20 eV to zero frequency. The evaluation was carried out as Z_{eff} = 25.48. Similar sum rules hold for the charge-carriers and bound electrons per atom. They can be evaluated using the decomposition of the ELF to obtain the effective number of charge-carriers contributing to conduction [$Z_{eff}^{(cc)}$], as well as the effective number of bound electrons participating in interband transitions [$Z_{eff}^{(it)}$]:

$$Z_{eff}^{(cc)} = \frac{2}{\pi\Omega_{pe}^2}\int_0^{\Omega_{\max}} \Omega \cdot L_D^{(B)}(\Omega)d\Omega, \quad (5a)$$

$$Z_{eff}^{(it)} = \frac{2}{\pi\Omega_{pe}^2}\int_0^{\Omega_{\max}} \Omega \cdot L_L^{(B)}(\Omega)d\Omega. \quad (5b)$$

Furthermore, the ELF associated with the bulk Lorentz contribution to the DF can be decomposed to display the relevant absorption peaks of each oscillator and the presence of collective oscillations of bound electrons. The starting point is the following equation

$$\frac{1}{\varepsilon_L(\Omega)} = \frac{A_j^{(B)}(\Omega)}{\varepsilon_{L,j}(\Omega)} + \frac{B_j^{(B)}(\Omega)}{\sum_{i=j+1}^{K}\varepsilon_{L,i}(\Omega)}, \quad (6)$$

with j = 1,2, …, *K*-1, where the real coefficients $A_j^{(B)}$ and $B_j^{(B)}$ are obtained by solving Equation (6) for their real and imaginary components. From them, the ELFs of each one of the first j-1 oscillators are given by

$$L_{L,j}^{(B)}(\Omega) = -\left[\prod_{i=0}^{j-1} B_i^{(B)}(\Omega)\right] A_j^{(B)}(\Omega) \cdot \mathrm{Im}\left[\frac{1}{\varepsilon_{L,j}(\Omega)}\right], \quad (7a)$$

and for the last K^{th} oscillator

$$L_{L,K}^{(B)}(\Omega) = -\left[\prod_{i=0}^{K-2} B_i^{(B)}(\Omega)\right] B_{K-1}^{(B)}(\Omega) \cdot \mathrm{Im}\left[\frac{1}{\varepsilon_{L,j}(\Omega)}\right], \quad (7b)$$

In this way, $L_L^{(B)}(\Omega) = \sum_{j=1}^{K} L_{L,j}^{(B)}(\Omega)$. The effective number of electrons per atom participating in each interband transition can be evaluated from the decomposition of the Lorentz ELF:

$$Z_{eff}^{(j)} = \frac{2}{\pi\Omega_{pe}^2} \int_0^{\Omega_{\max}} \Omega \cdot L_{L,j}^{(B)}(\Omega) d\Omega \,. \tag{8}$$

Other parameter that one can evaluate from the ELF is the dimensionless square of the dipole-matrix-element (DME) for all possible inelastic scattering processes within the spectral range considered [85, 87, 88]:

$$M_{tot}^2 = \frac{2R_\infty}{\pi\Omega_{pe}^2} \int_0^{\Omega_{\max}} \mathrm{Im}[-\frac{1}{\varepsilon(\Omega)}] d\Omega = \frac{2R_\infty}{\pi\Omega_{pe}^2} \int_0^{\Omega_{\max}} L^{(B)}(\Omega) d\Omega \,, \tag{9}$$

where R_∞ is the Rydberg constant (R_∞ = 13.6057 eV). This DME parameter has been defined as a dimensionless one by dividing the summation of individual DMEs between ea_oE_o where a_o is Bohr's radius and E_o is the modulus of the amplitude of the incident field (see Equation 2.11 in [88]). From the decompositions performed, the square of DMEs corresponding to the charge-carriers, bound electrons, and individual oscillators can also be evaluated:

$$M_D^2 = \frac{2R_\infty}{\pi\Omega_{pe}^2} \int_0^{\Omega_{\max}} L_D^{(B)}(\Omega) d\Omega \,, \tag{10a}$$

$$M_L^2 = \frac{2R_\infty}{\pi\Omega_{pe}^2} \int_0^{\Omega_{max}} L_L^{(B)}(\Omega) d\Omega \,, \tag{10b}$$

$$M_{L,j}^2 = \frac{2R_\infty}{\pi\Omega_{pe}^2} \int_0^{\Omega_{\max}} L_{L,j}^{(B)}(\Omega) d\Omega \,. \tag{10c}$$

The evaluations reported in Table 5 show that $Z_{eff} = Z_{eff}^{(cc)} + Z_{eff}^{(it)}$, $Z_{eff}^{(cc)} \cong z_e + z_h$ = 0.586, $M_{tot}^2 = M_D^2 + M_L^2$, and

$$Z_{eff}^{(it)} = \sum_{j=1}^{K} Z_{eff}^{(j)} \,, \qquad M_L^2 = \sum_{j=1}^{K} M_{L,j}^2 \,. \tag{10d}$$

A comparison of the $Z_{eff}^{(j)}$ values with the corresponding f_j and γ_j parameters show that a larger absorption width and the oscillator strength, which is proportional to the square of the dipole-matrix-element associated with the specific probability of transition, is associated with a larger effective number of electrons per atom participating in the j^{th} interband transitions.

Table 5 Set of derived quantities corresponding to effective numbers of charge-carriers (bound electrons) per atom doing intraband (interband) transitions in the spectral range considered, 0.2 to 40 eV, as well as the square of the dimensionless dipole-matrix-elements

Parameter	Value	Parameter	Value
$Z_{eff}^{(cc)}$	0.603	M_{tot}^2	12.53
$Z_{eff}^{(it)}$	24.88	M_D^2	0.278
$Z_{eff}^{(1)}$	0.043	M_L^2	12.25
$Z_{eff}^{(2)}$	0.084	$M_{L,1}^2$	0.037
$Z_{eff}^{(3)}$	0.021	$M_{L,2}^2$	0.075
$Z_{eff}^{(4)}$	0.928	$M_{L,3}^2$	0.022
$Z_{eff}^{(5)}$	0.040	$M_{L,4}^2$	0.718
$Z_{eff}^{(6)}$	1.671	$M_{L,5}^2$	0.050
$Z_{eff}^{(7)}$	11.08	$M_{L,6}^2$	1.217
$Z_{eff}^{(8)}$	11.01	$M_{L,7}^2$	5.533
----	----	$M_{L,8}^2$	4.600

8. Densities of States at the Final States Involved in Interband Transitions

For a given j[th] transition between bands, the absorption rate of energy can be obtained from Fermi's golden rule times the absorbed energy Ω_j [89]. The golden rule states that the transition rate is proportional to the density of states of the final states involved in the transition and the square matrix element of the Hamiltonian associated with the perturbation of the system due to the interaction between the propagating electric field and the induced dipoles. We have approached this square Hamiltonian matrix element in terms of $(ea_oE_o)^2M_j^2$. In classical electrodynamics, the absorption rate of energy corresponding to the j[th] oscillator, at the resonance frequency ω_j, and within the framework devised to decompose the Lorentz ELF in terms of those corresponding to each oscillator, is proportional to the corresponding j[th] ELF [81]. By considering the formulation of these two approaches for the rate of absorption as equal, the following equation is obtained

$$\frac{(2\pi)^2}{\mathrm{h}}\left[M_j^2(ea_oE_o)^2\right]\rho(E_j)\Delta E_j = \varepsilon_o E_o^2\left(\frac{2\pi\Omega_j}{h}\right)\mathrm{Im}\left[-\frac{C_j^{(B)}(\Omega_j)}{\varepsilon_{L,j}(\Omega_j)}\right], \tag{11}$$

with $\Delta E_j = E_j - E_{b,j}$ where E_j is the energy of the final state, and $E_{b,j}$ is the energy in the initial state of the transition, with $\Delta E_j \simeq \Omega_j$. Moreover

$$C_j^{(B)}(\Omega_j) = \left[\prod_{i=0}^{j-1} B_i^{(B)}(\Omega_j)\right] A_j^{(B)}(\Omega_j), \tag{12}$$

as indicated above. In this way, we obtained the following expression for the density of states at the final states involved in the transitions:

$$\rho(\Omega_j) = \frac{\varepsilon_o}{2\pi(ea_o)^2 M_j^2} \mathrm{Im}\left[-\frac{C_j^{(B)}(\Omega_j)}{\varepsilon_{L,j}(\Omega_j)}\right](2V_{pc}), \tag{13}$$

where $\rho(E_j) \simeq \rho(\Omega_j)$. The volume of the primitive unit cell (V_{pc}) was introduced in Equation (13) to obtain the density of states in units of states/energy atom, and a factor of 2 was added to account for the two accessible spin states of each electron. Table 6 shows the evaluations of the densities of states.

Table 6 Densities of states (in states/eV atom) at final states associated with each effective set of interband transitions

Parameter	Value	Parameter	Value
$\rho(\Omega_1)$	0.001	$\rho(\Omega_5)$	0.046
$\rho(\Omega_2)$	0.010	$\rho(\Omega_6)$	0.015
$\rho(\Omega_3)$	0.032	$\rho(\Omega_7)$	0.006
$\rho(\Omega_4)$	0.005	$\rho(\Omega_8)$	0.015

We finished our analysis with a comparison of the estimated $\rho(\Omega_j)$-values with those obtained from the DFT calculations reported in Section 3. Figure 6 and Figure 7 show the BSD displayed through an energy range larger than that used in Figure 1 and Figure 2. The right sides of these figures show the DOS using a logarithmic scale, which is appropriate to observe the orders of magnitudes of the densities of states when final states correspond to *s*, *p*, *d*, or *f* states, first for DTF calculations with no spin-orbit coupling and subsequently accounting for it, respectively. Through what follows, we compared the values obtained for $\rho(\Omega_j)$, as reported in Table 6, with corresponding values $\rho(E_j)$ estimated from the BSD when the energy of the final states (E_j) was projected toward the DOS in Figure 6 or Figure 7. We showed to aim that the $\rho(\Omega_j)$-values are consistent in order of magnitude with those of $\rho(E_j)$ when considering plausible transitions displayed in the BSD. Although our analysis is not intended to be exhaustive, it provides a significant degree of confidence in the method devised to obtain the $\rho(\Omega_j)$-values. We first considered the low-energy infrared transitions. According to the BSD displayed in Figure 2(a), the first resonance energy Ω_1 = 0.42 eV could arise from transitions between parallel bands displayed when approaching the L-symmetry point from the left, in the Λ-L direction (see Figure 8(a)). The light absorption due to these transitions was weak according to the low value of $f_1\gamma_1$. From the APCSA optimization, the $f_j\gamma_j$ values were between 0.17 and 66.3, with $f_1\gamma_1$ = 0.38. Electrons with energies between around 0.55 eV below and 0.53 eV above the SFL could participate in these transitions, showing that the largest density of states for the transitions with final states above the Fermi level (see the small peak of the s-DOS green line just above the SFL in Figure 6), i.e., ΔE_1 was about 0.54 eV. This largest peak value was close to $\rho(E_1)$ = 0.9×10^{-3} states/eV atom, which is of the same order of magnitude as $\rho(\Omega_1)$ = 0.001 states/eV atom if one considered that the electrons are transitioning into *p*-states. The bound electrons involved in these transitions could be *sp*- or *d*-electrons, according to Figure 2(b) and Figure 2(c), depending on

two factors: the number of *d*-electrons participating in these transitions is significantly larger than that of *sp*-electrons; however, *d*-states are more localized than *sp* and *p* states.

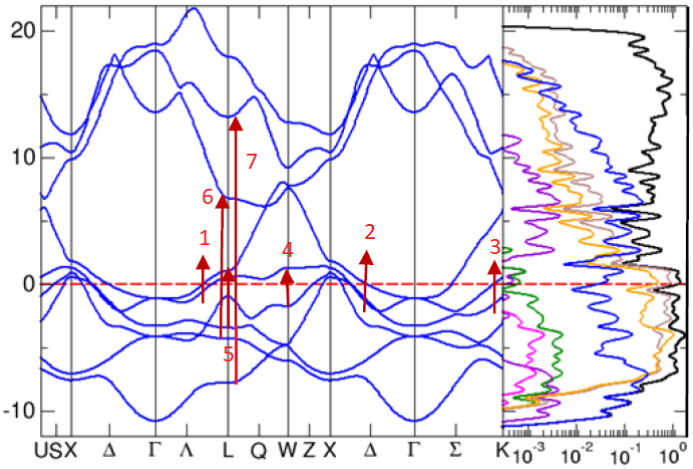

Figure 6 The BSD of Ir (left figure) and its total DOS (black line in right figure) and projected densities of states for *s* (violet line, j = 1/2), *p* (green and pink lines, j = 3/2 and j = 1/2, respectively), *d* (clear brown and yellowish lines, j = 5/2 and j = 3/2, respectively), and *s* with no spin-orbit coupling (blue line) states, in units of states/eV atom. The vertical scale on the left side is the energy in eV. The 0 energy (red dashed line) indicates the SFL. Except for the blue line of the DOS, the calculations included spin-orbit coupling. The numbered red arrows are used throughout the discussion in the text to indicate plausible interband transitions.

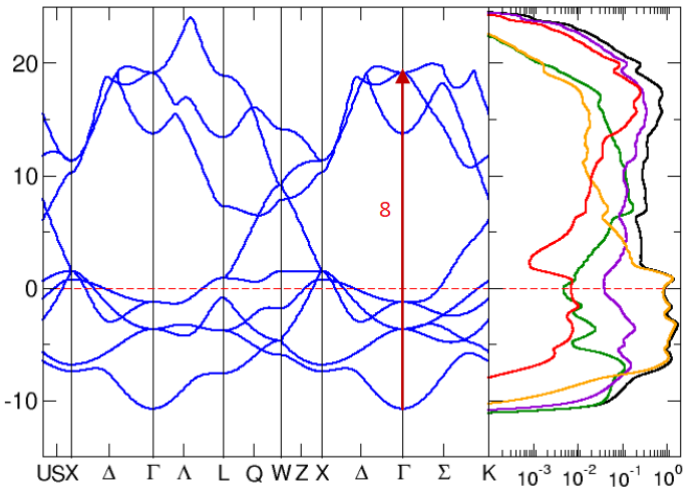

Figure 7 The BSD of Ir (left figure) and its total DOS (black line in right figure) and projected densities of states for *s* (green line), *p* (violet), *d* (yellowish), and *f* (red) states, in units of states/eV atom. The vertical scale on the left side is the energy in eV. The 0 energy (red dashed line) indicates the SFL. The spin-orbit coupling has not been accounted for. The red arrow with label 8 is used through the discussion in the text to indicate a plausible interband transition.

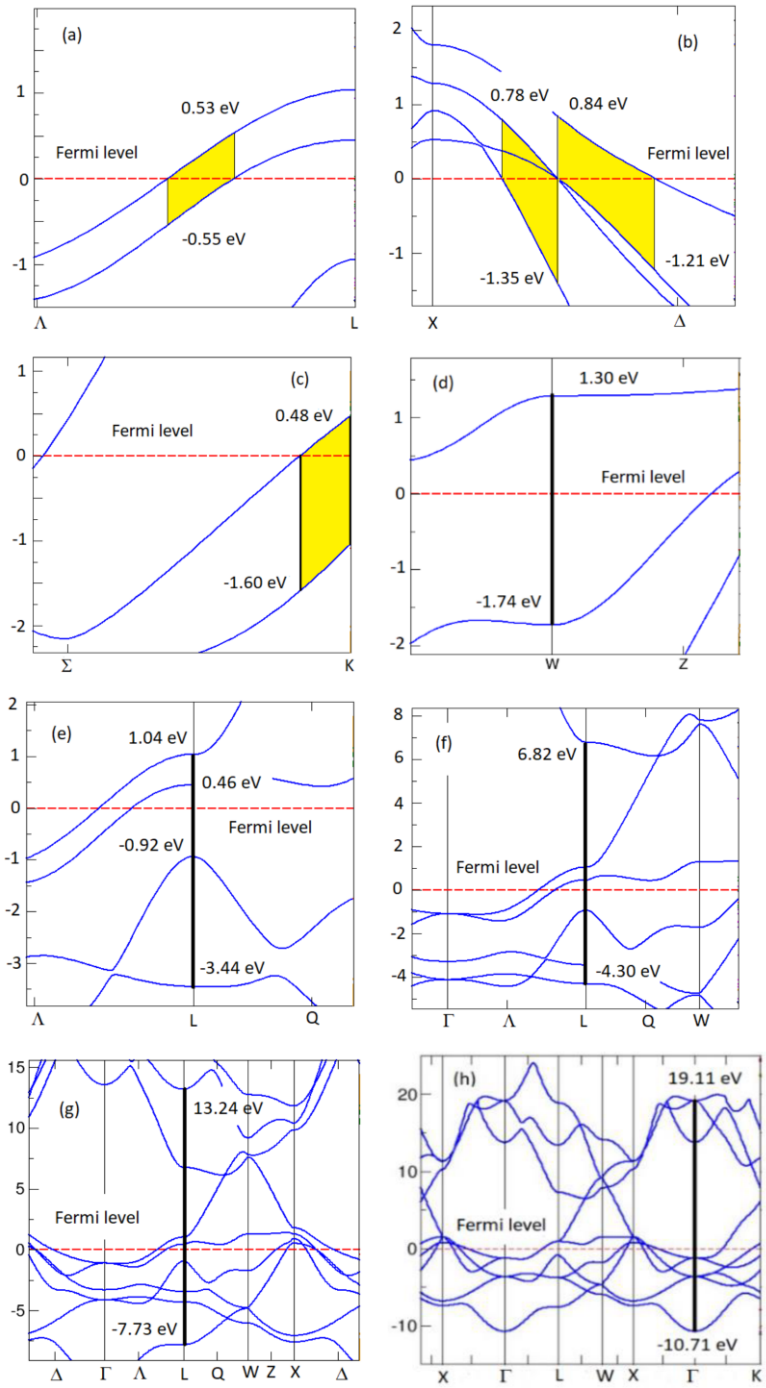

Figure 8 Amplified views of the BSD to show in detail the bands involved in the plausible transitions of bound electrons. The vertical scales are given in eV.

Regarding the second set of inter-band transitions, whose energy difference was close to Ω_2 = 1.21 eV with $f_2\gamma_2$ = 0.73, these could be located when going from the Δ- to the X-symmetry point, close to the middle point where two almost superposed bands cross the SFL having a band just below them and another just above (see Figure 8(b)). At the point where the two superimposed bands crosse the SFL $E_{b,2}$ = -1.35 eV, E_2 = 0 eV, and $\rho(E_2)$ = 0.028 states/eV atom if we assumed that these excitations involved *sp*-electrons transitioning to *s*-states with no spin-orbit coupling (see the blue line in Figure 7), according to the low value of $f_2\gamma_2$ = 0.73. At the left side of the point where the two superposed bands cross the SFL, E_2 = 0.78 eV, $E_{b,2}$ = 0 eV, and $\rho(E_2)$ = 0.055 states/eV atom.

These two estimations of $\rho(E_2)$ have the same order of magnitude as the value obtained from the APCSA approach, $\rho(\Omega_2)$ = 0.010 states/eV atom.

The density of states of the third set of transitions was evaluated in $\rho(\Omega_3)$ = 0.032 states/eV atom, with $f_3\gamma_3$ = 0.17 and Ω_3 = 2.07 eV. These could be attributed to transitions in the K-symmetry point, also involving the two parallel bands displayed from K to Σ (see Figure 8(c)). The energy below the SFL, with available empty states just above, can be estimated from $E_{b,3}$ = -1.60 eV, and the energy just above the SFL in the K point was close to E_3 = 0.48 eV above the SFL, i.e., ΔE_3 = 2.08 eV, and the value of $\rho(E_3)$ was between 0.028 and 0.041 states/eV atom, also assuming that *sp*-electrons were excited to *s*-states with no spin-orbit coupling, as observed, $\rho(E_3) \simeq \rho(\Omega_3)$. Other transitions that could be contributing to this set are displayed in the L-symmetry point, between the bands 0.92 eV below and 1.04 above the SFL (see Figure 8(e)). If the transitions of these *sp*-electrons are into *p*- or *s*-states with no spin-orbit coupling, the density of states would be the order of 0.001 or about 0.095 states/eV atom, respectively.

For the transition sets associated with Ω_4 = 3.22 eV, the density of final states was calculated as $\rho(\Omega_4)$ = 0.005 states/eV atom. According to Figure 8(d), this set of transitions could occur in the W-point between the band closer to the SFL, at $E_{b,4}$ = 1.74 eV below, and the upper band at E_4 = 1.30 eV above (ΔE_4 = 3.04 eV). The projection of the E_4-energy toward the DOS spectrum indicates that the density of states would be between 0.0004 and 0.032 states/eV atom, depending on the characteristic of the final states: *p*-states with j = 1/2 and j = 3/2 or *s*-states with no coupling between the spin and angular momentum of the electrons, respectively. The intermediate value of $f_4\gamma_4$ = 8.38 and the bands displayed in Figure 2(b) and (c) at the W-symmetry point suggested that both *sp*- and *d*-electrons participated in these transitions.

The fifth set of transitions corresponded to an energy difference of about Ω_5 = 4.38 eV, with a density of states $\rho(\Omega_5)$ = 0.046 states/eV atom for the final states. Transitions in the L-point between bands separated by the energy difference $\Delta E_5 = E_5 - E_{b,5}$ = 4.48 eV, with E_5 = 1.04 eV above the SFL and $E_{b,5}$ = 3.44 eV below it (see Figure 8(e)). The projection of the E_5-value toward the DOS figure showed that the density of states could be around $\rho(E_5)$ = 0.088 states/eV atom involving the transitions of *sp*-electrons to *s*-states with no spin-orbit coupling, which would be consistent with the low value of $f_5\gamma_5$ = 0.24. Other transitions that contribute to this set could be occurring up to the band 0.46 eV above the SFL. In that case, $\rho(E_5)$ = 0.041 states/eV atom.

We finally considered the transitions at the vacuum ultraviolet, which are characterized by large values of $f_j\gamma_j$. The effective sixth set of transitions was characterized by a resonance energy Ω_6 = 11.10 eV with a density of states $\rho(\Omega_6)$ = 0.015 states/eV atom. According to the BSD depicted in Figure 8(f), plausible transitions at the L-point whose energy difference was $\Delta E_6 = E_6 - E_{b,6}$ = 11.12 eV, with E_6 = 6.82 eV above the Fermi level and $E_{b,6}$ = 4.30 eV below, and a corresponding density of states close to $\rho(E_6)$ = 0.013 states/eV which corresponded to *d*-electrons transitioning to *d*-states (with j = 3/2). This is consistent with the BSDs of Figure 2(b) and Figure 2(c) and with a large value of $f_6\gamma_6$ = 10.08.

For the seventh set of transitions, Ω_7 = 19.43 eV with $\rho(\Omega_7)$ = 0.006 states/eV atom. The BSD showed plausible transitions at the L-direction from the lower band at $E_{b,7}$ = 7.73 eV below the Fermi level up to the upper band at E_7 = 13.24 eV above, i.e., ΔE_7 = 20.97 eV (see Figure 8(g)). At this E_7-spectral position, the DOS in Figure 6 indicated that final *d*-states (with j = 5/2) were involved in these transitions with a density of states close to $\rho(E_7)$ = 0.004 states/eV atom and with initial *d*-states.

For the eighth set of transitions, we used the information displayed in Figure 7. The resonance frequency was estimated as Ω_8 = 31.17 eV with the density of states $\rho(\Omega_8)$ = 0.015 states/eV atom. According to Figure 8(h), the BSD showed plausible transitions at the Γ-point from the lower band at $E_{b,8}$ = 10.71 eV below the Fermi level up to the upper band at E_8 = 19.11 eV above the Fermi level, i.e., ΔE_8 = 29.82 eV. At this E_8-spectral position, the DOS figure indicated that final *f*-states were involved in these transitions of *d*-electrons, with a density of states close to $\rho(E_8)$ = 0.070 states/eV.

When the transitions involved only *p*-electrons, the density of states approached the 0.1 states/eV atom value. Close to this Γ-point, in the Δ-direction, there was a section where one could see parallel bands contributing to this effective set of transitions, with decreasing densities of states up to about 0.010 states/eV atom. According to the value obtained for $\rho(\Omega_8)$, these transitions contributed more significantly and involved *s*- and *d*-electrons.

We finished the analysis correlating the spectral composition of the DF's imaginary component with the set of interband transitions displayed in previous figures. Figure 9(a) shows the spectrum of ε_2 with an indication of spectral positions of the resonance energies and the symmetry points or parallel bands involved in the quantum transitions of bound electrons. Figure 9(b) displays the decomposition of the Lorentz contribution to the DF as provided by each set of transitions.

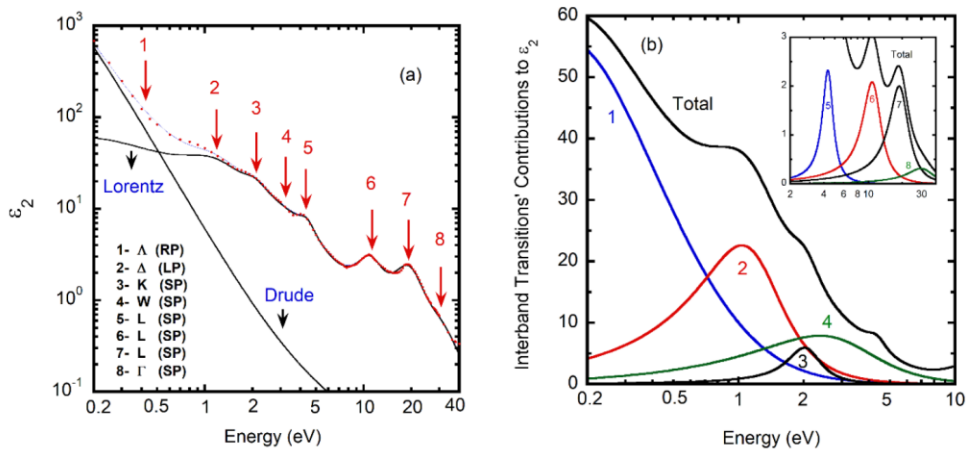

Figure 9 (a) Imaginary component of Ir's DF indicating that the spectral positions of the resonances energies correlated with the transitions indicated in the inset: RP (LP) means right (left) side of the Λ (Δ) point involving parallel (quasi-parallel) bands, and SP means symmetry point. The bands involved in the transitions have been indicated in the two previous figures. Dots are the original data taken from [20], and the solid line displays the evaluation from the set of optimized parameters specified in Table 2. (b) The contribution of each set of interband transitions to the DF of Ir.

9. Summary and Conclusions

A framework to model the dielectric function of transition metals has been devised, with Ir as the material considered in this work. The model is an extended version of the Drude–Lorentz model, which incorporates the contribution of holes as charge-carriers. The complete set of model parameters was optimized using a simulated annealing approach assisted by a projected gradient method. The physical meaning of the model parameters was emphasized, going beyond a simple fitting procedure. Several derived quantities were obtained once the optimization procedure was

finished, and additional optical, charge transport, magnetic, and quantum mechanical properties of the material were reported. Background knowledge was provided by Density Functional Theory calculations, including spin-orbit coupling. Within this background, a consistent interpretation of Fermi energies and density of states at Fermi energies of holes and electrons was provided. In addition to the parametric spectral description of the dielectric function, other optical parameters are obtained from the optimization process or as derived quantities: plasma frequency of s-conduction electrons, effective plasma frequency of both charge carriers (holes and electrons), intrinsic relaxation times of holes and electrons, high-frequency dielectric constant, the number density of electrons and holes, and their effective masses. The optical response of bound electrons was required to optimize the values of oscillator strengths, resonance energies, and absorption widths. Furthermore, several charge transport properties were obtained as derived quantities both for electrons and holes: Fermi velocities, intrinsic mean free paths, mobilities, static conductivity, dynamic conductivity contributions, Hall's coefficient, intrinsic resistivity, and heat capacities. The magnetic properties evaluated included Pauli's paramagnetic and Landau's diamagnetic susceptibilities for electrons and holes. In addition, a large set of quantum mechanical parameters were evaluated: charge-carriers Fermi energies and corresponding densities of states at the Fermi energy. A first decomposition of the energy loss function allowed us to calculate the effective numbers of itinerant charge carriers participating in inter- or intra-band transitions through the spectral range considered, as well as the total effective numbers of bound electrons doing interband transitions. From a second decomposition, focused on the Lorentz contribution to the ELF, a model was devised to obtain the energy loss functions associated with each set of transitions. From these oscillator ELFs, the characteristic of the participating electrons (*s*, *p*, *d*, or *f*) was established, and the density of states at the final states involved in these transitions was calculated. Comparisons of these densities of states with the data provided by the DFT calculations showed good agreement in terms of their orders of magnitude.

Acknowledgments

The authors thank the support given by the Universidad de Costa Rica to carry out this research. They also thank Professor Gunnar A. Niklasson, at Uppsala University, Sweden, for reading the manuscript and for his valuable comments.

Author Contributions

Implementation of the SPGM + APCSA programs (WE Vargas), application of the SPGM + APCSA method for modeling the DF of Ir (WE Vargas, M Hernández-Jiménez, and V Quirós-Cordero), DFT calculations (F Muñoz-Rojas and E Avendano), and manuscript preparation (WE Vargas).

Competing Interests

The authors have declared that no competing interests exist.

Appendix: Optimization by a Spectral Projected Gradient Method

The SPGM requires initial input values for the parameters being optimized. They are obtained from previous applications at each temperature cycle of the APCSA method to minimize the merit function *F* specified by Equation (2), which can be written as $F = F_o \sum_{i=1}^{\kappa}(F_{1,i}^2 + F_{2,i}^2)$ with

$$F_{1,i}(\Omega_i) = \left[\frac{\varepsilon_1(\Omega_i)}{\bar{\varepsilon}_1(\Omega_i)}\right] - 1 \text{ and } F_{2,i}(\Omega_i) = \frac{\varepsilon_2(\Omega_i)}{\bar{\varepsilon}_2(\Omega_i)} - 1$$

where the constant factor is given by $F_o = (2\kappa - N_p - 1)^{-1}$. The explicit forms of ε_1 and ε_2 are obtained from Equation (1), namely,

$$\varepsilon_1(\Omega) = \frac{1}{f_o} - \frac{\Omega_{pe}^2}{\Omega^2 + \gamma_e^2} - \frac{\chi\beta\Omega_{pe}^2}{\Omega^2 + \gamma_h^2} + \varepsilon_{1,L}, \qquad \varepsilon_2(\Omega) = \frac{\gamma_e\Omega_{pe}^2}{\Omega(\Omega^2 + \gamma_e^2)} + \frac{\chi\beta\gamma_h\Omega_{pe}^2}{\Omega(\Omega^2 + \gamma_h^2)} + \varepsilon_{2,L} \quad \text{(A1)}$$

with

$$\varepsilon_{1,L} = \frac{1}{z_e}\sum_{j=1}^{K}\frac{f_j\Omega_{pe}^2(\Omega_j^2 - \Omega^2)}{(\Omega_j^2 - \Omega^2)^2 + (\Omega\gamma_j)^2}, \qquad \varepsilon_{2,L} = \frac{1}{z_e}\sum_{j=1}^{K}\frac{f_j\Omega_{pe}^2\Omega\gamma_j}{(\Omega_j^2 - \Omega^2)^2 + (\Omega\gamma_j)^2}. \quad \text{(A2)}$$

The chain rule was applied to evaluate the components of the gradient, which requires the previous evaluation of $dF_{1,i}/d\varepsilon_1$ and $dF_{2,i}/d\varepsilon_2$. If *p* is one of the N_p parameters under optimization,

$$\frac{dF}{dp} = 2F_o\sum_{i=1}^{\kappa}F_{1,i}(\Omega_i)\left(\frac{dF_{1,i}}{d\varepsilon_1}\right)\left(\frac{d\varepsilon_1}{dp}\right)_{\Omega_i} + 2F_o\sum_{i=1}^{\kappa}F_{2,i}(\Omega_i)\left(\frac{dF_{2,i}}{d\varepsilon_2}\right)\left(\frac{d\varepsilon_2}{dp}\right)_{\Omega_i}, \quad \text{(A3)}$$

with $dF_{1,i}/d\varepsilon_1 = 1/\bar{\varepsilon}_1(\Omega_i)$ and $dF_{2,i}/d\varepsilon_2 = 1/\bar{\varepsilon}_2(\Omega_i)$. The non-null derivates of ε_1 and ε_2 respect to each optimization parameter are specified in Table A1.

Table A1 Derivatives with respect to parameters related to the Drude contribution to the dielectric function, and with respect to z_e parameter involved in the Lorentz term.

$\frac{d\varepsilon_1}{d\Omega_{pe}} = 2(\varepsilon_1 - 1/f_o)/\Omega_{pe}$	$\frac{d\varepsilon_2}{d\Omega_{pe}} = 2\varepsilon_2/\Omega_{pe}$	$\frac{d\varepsilon_1}{df_o} = -1/f_o^2$
$\frac{d\varepsilon_1}{d\gamma_{oe}} = \frac{d\varepsilon_1}{d\gamma_e}\frac{d\gamma_e}{d\gamma_{oe}} + \frac{d\varepsilon_1}{d\gamma_h}\frac{d\gamma_h}{d\gamma_{oe}}$	$\frac{d\varepsilon_1}{d\gamma_e} = \frac{2\gamma_e\Omega_{pe}^2}{(\Omega^2 + \gamma_e^2)^2}$	$\frac{d\varepsilon_1}{d\gamma_h} = \frac{2\gamma_h\chi\beta\Omega_{pe}^2}{(\Omega^2 + \gamma_e^2)^2}$
$\frac{d\gamma_e}{d\gamma_{oe}} = \frac{\gamma_e}{\gamma_{oe}}$	$\frac{d\gamma_h}{d\gamma_{oe}} = \frac{\gamma_h}{\gamma_{oe}}$	$\frac{d\varepsilon_2}{d\gamma_{oe}} = \frac{d\varepsilon_2}{d\gamma_e}\frac{d\gamma_e}{d\gamma_{oe}} + \frac{d\varepsilon_2}{d\gamma_h}\frac{d\gamma_h}{d\gamma_{oe}}$
$\frac{d\varepsilon_2}{d\gamma_e} = \frac{\Omega_{pe}^2(\Omega^2 - \gamma_e^2)}{\Omega(\Omega^2 + \gamma_e^2)^2}$	$\frac{d\varepsilon_2}{d\gamma_h} = \frac{\chi\beta\Omega_{pe}^2(\Omega^2 - \gamma_h^2)}{\Omega(\Omega^2 + \gamma_h^2)^2}$	$\frac{d\varepsilon_1}{d\eta} = \frac{d\varepsilon_1}{d\gamma_h}\frac{d\gamma_h}{d\eta} + \frac{d\varepsilon_2}{d\gamma_h}\frac{d\gamma_h}{d\eta}$
$\frac{d\gamma_h}{d\eta} = \frac{\gamma_h}{\eta}$	$\frac{d\varepsilon_1}{d\beta} = -\frac{\chi\Omega_{pe}^2}{\Omega^2 + \gamma_h^2}$	$\frac{d\varepsilon_2}{d\beta} = \frac{\chi\gamma_h\Omega_{pe}^2}{\Omega(\Omega^2 + \gamma_h^2)}$

$\frac{d\varepsilon_1}{dz_e} = -\frac{1}{z_e}\varepsilon_{1,L}$	$\frac{d\varepsilon_2}{dz_e} = -\frac{1}{z_e}\varepsilon_{2,L}$	$\frac{d\varepsilon_1}{d\chi} = -\frac{\beta\Omega_{pe}^2}{\Omega^2+\gamma_h^2}$
$\frac{d\varepsilon_2}{d\chi} = \frac{\beta\gamma_h\Omega_{pe}^2}{\Omega(\Omega^2+\gamma_h^2)}$	$\frac{d\varepsilon_1}{d\Gamma_h} = \frac{d\varepsilon_1}{d\gamma_h}\frac{d\gamma_h}{d\Gamma_h}$	$\frac{d\varepsilon_2}{d\Gamma_h} = \frac{d\varepsilon_2}{d\gamma_h}\frac{d\gamma_h}{d\Gamma_h}$
$\frac{d\gamma_h}{d\Gamma_h} = -2\frac{\gamma_{oh}}{\Gamma_h}\left(\frac{\gamma_h}{\gamma_{oh}}-1\right)$	$\frac{d\varepsilon_1}{d\Gamma_e} = \frac{d\varepsilon_1}{d\gamma_e}\frac{d\gamma_e}{d\Gamma_e}$	$\frac{d\varepsilon_2}{d\Gamma_e} = \frac{d\varepsilon_2}{d\gamma_e}\frac{d\gamma_e}{d\Gamma_e}$
$\frac{d\gamma_e}{d\Gamma_e} = -2\frac{\gamma_{oe}}{\Gamma_e}\left(\frac{\gamma_e}{\gamma_{oe}}-1\right)$		

For the optimization parameters involved in the Lorentz term, we used the following expressions for the corresponding derivates related to the j[th] oscillator's contribution:

Table A2 Derivatives with respect to parameters related to the Lorentz contribution to the dielectric function

$\frac{d\varepsilon_1}{df_j} = \frac{1}{z_e}\frac{\Omega_{pe}^2(\Omega_j^2-\Omega^2)}{(\Omega_j^2-\Omega^2)^2+(\Omega\gamma_j)^2}$	$\frac{d\varepsilon_2}{df_j} = \frac{1}{z_e}\frac{\Omega_{pe}^2\Omega\gamma_j}{(\Omega_j^2-\Omega^2)^2+(\Omega\gamma_j)^2}$
$\frac{d\varepsilon_1}{d\Omega_j} = \frac{2}{z_e}\frac{f_j\Omega_j\Omega_{pe}^2\left[(\Omega\gamma_j)^2-(\Omega_j^2-\Omega^2)^2\right]}{\left[(\Omega_j^2-\Omega^2)^2+(\Omega\gamma_j)^2\right]^2}$	$\frac{d\varepsilon_2}{d\Omega_j} = -\frac{4}{z_e}\frac{f_j\gamma_j\Omega_j\Omega_{pe}^2\Omega(\Omega_j^2-\Omega^2)}{\left[(\Omega_j^2-\Omega^2)^2+(\Omega\gamma_j)^2\right]^2}$
$\frac{d\varepsilon_1}{d\gamma_j} = -\frac{2}{z_e}\frac{f_j\gamma_j\Omega_{pe}^2(\Omega_j^2-\Omega^2)\Omega^2}{\left[(\Omega_j^2-\Omega^2)^2+(\Omega\gamma_j)^2\right]^2}$	$\frac{d\varepsilon_2}{d\gamma_j} = \frac{f_j\Omega_{pe}^2\Omega\left[(\Omega_j^2-\Omega^2)^2-(\Omega\gamma_j)^2\right]}{z_e\left[(\Omega_j^2-\Omega^2)^2+(\Omega\gamma_j)^2\right]^2}$

References

1. Hunt LB. A history of iridium. Platinum Metals Rev. 1987; 31: 32-41.
2. Shirvaliloo S, Kangarloo H. Production of iridium metal thin films for application as electrodes in DRAMs and FRAMs. J Electr Electron Eng. 2015; 3: 35-38.
3. Youm M, Sim HS, Jeon H, Kim S, Kim YT. Metal oxide semiconductor field effect transistor characteristics with iridium gate electrode on atomic layer deposited ZrO_2 high-k dielectrics. Jpn J Appl Phys. 2003; 42: 5010-5013.
4. Wang YF, Chang X, Li S, Zhao D, Shao G, Zhu T, et al. Ohmic contact between iridium film and hydrogen-terminated single crystal diamond. Sci Rep. 2017; 7: 12157.
5. Hemphill R, Hurwitz M, Pelizzo MG. Osmium atomic-oxygen protection by an iridium overcoat for increased extreme-ultraviolet grating efficiency. Appl Opt. 2003; 42: 5149-5157.
6. Ozaki Y. Temperature and humidity dependence of SnO_2-based CO gas sensors modified with iridium and ruthenium. Electrochem Solid-State Lett. 1999; 3: 297-299.
7. Blaser HU. Application of iridium catalysts in the fine chemicals industry. In: Iridium complexes in organic synthesis. Weinheim: Wiley-VCH Verlag GmbH & Co. KGaA; 2008. pp. 1-14.
8. Oro A, Claver C. Iridium catalysts for organic reactions. Cham: Springer Nature Switzerland AG; 2021.

9. John S, Wang R. Metallic photonic-band-gap filament architectures for optimized incandescent lighting. Phys Rev A. 2008; 78: 043809.
10. Wen RT, Niklasson GA, Granqvist CG. Strongly improved electrochemical cycling durability by adding iridium to electrochromic nickel oxide films. ACS Appl Mater Interfaces. 2015; 7: 9319-9322.
11. Sachse R, Pflüger M, Velasco-Vélez JJ, Sahre M, Radnik J, Bernicke M, et al. Assessing optical and electrical properties of highly active IrO_x catalysts for the electrochemical oxygen evolution reaction via spectroscopic ellipsometry. ACS Catal. 2020; 10: 14210-14223.
12. El Sayed AM, Shaban M. Morphological, surface and optical properties of spin-coated IrO_x films; influence of spin speed, annealing and (Cr, La) codoping. Ceram Int. 2019; 45: 8460-8470.
13. Coblentz WW. The reflecting power of various metals. Bull Bur Stand. 1910; 7: 197-225.
14. Barnes BT. Optical constants of incandescent refractory metals. J Opt Soc Am. 1966; 56: 1546-1550.
15. Hass G, Jacobus GF, Hunter WR. Optical properties of evaporated iridium in the vacuum ultraviolet from 500 Å to 2000 Å. J Opt Soc Am. 1967; 57: 758-762.
16. Samson JAR, Padur JP, Sharma A. Reflectance and relative transmittance of laser-deposited iridium in the vacuum ultraviolet. J Opt Soc Am. 1967; 57: 966-967.
17. Kirillova M, Nomerovannaya LV, Noskov MM. Optical properties of iridium at 77 and 295 K. Fiz Metal Metalloved. 1972; 34: 291-296.
18. Weaver JH. Optical properties of Rh, Pd, Ir, and Pt. Phys Rev B. 1975; 11: 1416-1425.
19. Weaver JH, Olson CG, Lynch DW. Optical investigation of the electronic structure of bulk Rh and Ir. Phys Rev B. 1977; 15: 4115-4118.
20. Weaver JH. Optical properties of metals. In: Handbook of chemistry and physics. 73rd ed. Boca Raton: CRC Press; 1993. pp. 111-126.
21. Windt DL, Cash WC, Scott M, Arendt P, Newnam B, Fisher RF, et al. Optical constants of thin films of Ti, Zr, Nb, Mo, Ru, Rh, Pd, Ag, Hf, Ta, W, Re, Ir, Os, Pt, and Au from 24 Å to 1216 Å. Appl Opt. 1988; 27: 246-278.
22. Yan L, Woollam JA. Optical constants and roughness study of dc magnetron sputtered iridium films. J Appl Phys. 2000; 92: 4386-4392.
23. Lehmuskero A, Kuittinen M, Vahimaa P. Refractive index and extinction coefficient dependence of thin Al and Ir films on deposition technique and thickness. Opt Express. 2007; 15: 10744-10752.
24. Yang LH, Menyhárd M, Sulyok A, Tokési K, Ding ZJ. Optical properties and excitation energies of iridium derived from reflection electron energy loss spectroscopy spectra. Appl Surf Sci. 2018; 456: 999-1003.
25. Krog-Andersen O. Fermi surfaces and effective masses in fcc transitions metals. Solid State Commun. 1968; 6: 285-290.
26. Krogh-Andersen O. Electronic structure of the fcc transition metals Ir, Rh, Pt, and Pd. Phys Rev B. 1970; 2: 883-906.
27. Arbman GO, Hornfelt S. Crystal potentials and the band electrons of iridium. J Phys F Metal Phys. 1972; 2: 1033-1045.
28. Noffke J, Fritsche L. Band structure calculation and photoemission analysis of iridium. J Phys F Metal Phys. 1982; 12: 921-933.

29. Choi WS, Seo SSA, Kim KW, Noh TW, Kim MY, Shin S. Dielectric constants of Ir, Ru, Pt, and IrO_2: Contributions from bound charges. Phys Rev B. 2006; 74: 205117.
30. Ahmed S, Zafar M, Shakil M, and Choudhary MA. Ab initio study of structural, electronic, and thermal properties of $Ir_{1-x}Rh_x$ alloys. Condens Matter Phys. 2015; 18: 23601.
31. Sigalas MM, Papaconstantopoulos DA. Calculations of the total energy, electron-phonon interaction, and Stoner parameter for metals. Phys Rev B. 1993; 50: 7255-7261.
32. Abarca-Quesada DA, Vargas-Quirós CE, Vargas WE. Physical properties of rhodium retrieved from modeling its dielectric function by a simulated annealing approach. OSA Continuum. 2021; 4: 3233-3253.
33. Vargas WE. Optical, magnetic, and charge-carriers transport properties of a transition metal: Bulk palladium. Appl Opt. 2017; 56: 6496-6503.
34. Vargas WE. Dielectric functions of Pd and Zr transition metals: An application of Drude-Lorentz models with simulated annealing optimization. Appl Opt. 2017; 56: 1266-1276.
35. Arblaster JW. Crystallographic properties of iridium. Platinum Metals Rev. 2010; 54: 93-102.
36. Volkenshtein NV, Novoselov VA, Startsev VE. The Fermi surface of iridium. Sov Phys JETP. 1970; 31: 862-863.
37. Theye ML. Investigation of the optical properties of Au by means of thin semitransparent films. Phys Rev B. 1970; 2: 3060-3078.
38. Nagel SR, Schnatterly SE. Frequency dependence of the Drude relaxation time in metal films. Phys Rev B. 1974; 9: 1299-1303.
39. Eisenhammer T. Photon frequency dependent electron relaxation time in noble metals: Effect of voids. Thin Solid Films. 1995; 270: 55-59.
40. Rakic AD, Elazar JM, Djurisic AB. Acceptance-probability-controlled simulated annealing: A method for modeling the optical constants of solids. Phys Rev E. 1995; 52: 6862-6867.
41. Rakic AD, Djurisic AB, Elazar JM, Majewski ML. Optical properties of metallic films for vertical-cavity optoelectronic devices. Appl Opt. 1998; 37: 5271-5283.
42. Kirkpatrick S, Gelatt CD, Vecchi MP. Optimization by simulated annealing. Science. 1983; 220: 671-680.
43. Raydan M. The Barzilai and Borwein gradient method for the large-scale unconstrained minimization problem. SIAM J Optim. 1997; 7: 26-33.
44. Ramírez-Porras A, Vargas WE. Transmission of visible light through oxidized copper films: Feasibility of using a spectral projected gradient method. Appl Opt. 2004; 43: 1508-1514.
45. Morrish AH. The physical principles of magnetism. New York: IEEE Press; 2001.
46. Ziman JM. Electrons and phonons. London: Oxford University Press; 1960.
47. Batyev EG. Pauli paramagnetism and Landau diamagnetism. Phys Usp. 2009; 52: 1245-1246.
48. Hamman DR, Schluter M, Chiang C. Norm-conserving pseudopotentials. Phys Rev Lett. 1979; 43: 1494-1497.
49. Kohn W, Sham LJ. Self-consistent equations including exchange and correlation effects. Phys Rev. 1964; 140: A1133-A1138.
50. Giannozzi P, Baroni S, Bonini N, Calandra M, Car R, Cavazzoni C, et al. QUANTUM ESPRESSO: A modular and open-source software project for quantum simulations of materials. J Phys Condens Matter. 2009; 21: 395502.
51. Perdew JP, Burke K, Ernzerhof M. Generalized gradient approximation made simple. Phys Rev Lett. 1996; 77: 3865-3868.

52. Zhang Y, Yang W. Comment on Generalized gradient approximation made simple. Phys Rev Lett. 1998; 80: 890.
53. Troullier N, Martins JL. Efficient pseudopotential for plane-wave calculations. Phys Rev B. 1991; 43: 1993-2006.
54. Singh HP. Determination of thermal expansion of germanium, rhodium, and iridium by X-rays. Acta Crystallogr Sect A. 1968; 24: 469-471.
55. Fischer M, Evers FO, Formalik F, Olejniczak A. Benchmarking DFT-GGA calculations for the structure optimisation of neutral-framework zeotypes. Theor Chem Acc. 2016; 135: 257.
56. Methfessel M, Paxton AT. High-precision sampling for Brillouin-zone integration in metals. Phys Rev B. 1989; 40: 3616-3621.
57. Monkhorst HJ, Pack JD. Special points for Brillouin-zone integrations. Phys Rev B. 1976; 13: 5188-5192.
58. Vargas WE, Clark N, Muñoz-Rojas F, Azofeifa DE, Niklasson GA. Optical, charge transport, and magnetic properties of Pd retrieved from photometric measurements: Approaching the quantum mechanics background. Phys Scr. 2019; 94: 055101.
59. Vuillemin JJ, Priestley MG. De Haas-van Alphen effect and Fermi surface in palladium. Phys Rev Lett. 1965; 14: 307-309.
60. Reale C. Determination of charge-transport parameters for the group IV metals. Re Bras Fís. 1973; 3: 431-439.
61. Meaden GT. Electrical resistance of metals. New York: Plenum Press; 1965.
62. Hurd CM. The hall effect in metals and alloys. New York: Plenum Press; 1972.
63. Powell RW, Tye RP, Woodman MJ. Thermal conductivities and electrical resistivities of the platinum metals. Platinum Met Rev. 1962; 6: 138-143.
64. Aisaka T, Shimizu M. Electrical resistance, thermal conductivity and thermoelectric power of transition metals at high temperatures. J Phys Soc Japan. 1970; 28: 646-654.
65. Hörnfeldt S, Hammarström Å, Carrander K, Björck G. The de Haas-van Alphen effect and the Fermi surface in iridium. J Phys Chem Solids. 1971; 32: 753-760.
66. Grodski JJ, Dixon AE. de Hass-van Alphen effect in iridium. Phys Rev B. 1972; 6: 1198-1209.
67. Albert HJ, Rubin LR. Magnetic properties of the platinum metals and their alloys. In: Platinum group metals and compounds. Washington: American Chemical Society; 1971. pp. 1-16.
68. Vosko SH, Perdew JP. Theory of the spin susceptibility of an inhomogenous electron gas via the density functional formalism. Can J Phys. 1975; 53: 1885-1897.
69. Allen PB. The electron-phonon coupling constant. In: Handbook of Superconductivity. New York: Academic Press; 1999. pp. 478-483.
70. Cahaya AB. Paramagnetic and diamagnetic susceptibility of infinite quantum well. J Mater Sci Geophys Instrum Theor Phys. 2020; 3: 61-67.
71. Lindhard J. On the properties of a gas of charge particles. Dan Mat Fys Medd. 1954; 28: 8.
72. Dorofeev IA, Vinogradov EA. Structure of electromagnetic fields near the surface of an ionic crystal. J Surf Investig. 2012; 6: 796-804.
73. Ashcroft NW, Mermin ND. Solid state physics. New York: Saunders College Publishing; 1976.
74. Furukawa GT, Reilly ML, Gallagher S. Critical analysis of heat-capacity data and evaluation of thermodynamics properties of ruthenium, rhodium, palladium, iridium, and platinum from 0 to 300 K. A survey of the literature data on osmium. J Phys Chem Ref Data. 1974; 3: 163-209.

75. McMillan WL. Transition temperature of strong-coupled superconductors. Phys Rev. 1968; 167: 331-344.
76. Stewart GR. Measurement of low-temperature specific heat. Rev Sci Instrum. 1983; 54: 1-11.
77. Luttinger JM, Ward JC. Ground-state energy of a many-fermion system. II. Phys Rev. 1960; 118: 1417-1427.
78. Kas JJ, Blanton TD, Rehr JJ. Exchange-correlation contributions to thermodynamic properties of the homogenous electron gas from a cumulant Green's function approach. Phys Rev B. 2019; 100: 195144.
79. Papaconstantopoulos DA. Handbook of the band structure of elemental solids. From Z = 1 to Z = 112. New York: Springer; 2015.
80. Mott NF, Fowler RH. The electrical conductivity of transition metals. Proc R Soc London Ser A. 1936; 153: 699-717.
81. Dressel M, Grüner G. Electrodynamics of solids. Cambridge: Cambridge University Press; 2003.
82. Sun Y, Xu H, Da B, Mao SF, Ding ZJ. Calculation of energy-loss function for 26 materials. Chinese J Chem Phys. 2016; 29: 663-670.
83. Madelung O. Introduction to solid-state theory. Berlin: Springer; 1996.
84. Tanuma S, Powell CJ, Penn DR. Use of sum rules on the energy-loss function for the evaluation of experimental optical data. J Electron Spectros Relat Phenomena. 1993; 62: 95-109.
85. Tanuma S, Powell CJ, Penn DR. Inelastic mean free paths of low-energy electrons in solids. Acta Phys Pol A. 1992; 81: 169-186.
86. Burden RL, Faires DJ, Burden AM. Numerical analysis. USA: Cengage Learning; 2015.
87. Fano U. Atomic theory of electromagnetic interactions in dense materials. Phys Rev. 1956; 103: 1202-1218.
88. Inokuti M. Inelastic collisions of fast charged particles with atoms and molecules—The Bethe theory revisited. Rev Mod Phys. 1971; 43: 297-347.
89. Bransden BH, Joachain CJ. Introduction to quantum mechanics. USA: Prentice Hall; 2000.